Eur. Phys. J. A **11**, 59–78 (2001)

**THE EUROPEAN PHYSICAL JOURNAL A**



# Modeling a neutron-rich nuclei source

M. Mirea[1,2,a], O. Bajeat[1], F. Clapier[1], F. Ibrahim[1], A.C. Mueller[1], N. Pauwels[1], and J. Proust[1]

[1] Institut de Physique Nucléaire, 91406, Orsay Cedex, France
[2] Institute of Physics and Nuclear Engineering, Tandem Lab., P.O.Box MG-6, Bucarest, Romania

Received: 1 December 2000 / Revised version: 19 March 2001
Communicated by D. Guerrau

**Abstract.** The deuteron break-up process in a suitable converter gives rise to intense neutron beams. A source of neutron-rich nuclei based on the neutron-induced fission can be realised using these beams. A theoretical optimization of such a facility as a function of the incident deuteron energy is reported. The model used to determine the fission products takes into account the excitation energy of the target nucleus and the evaporation of prompt neutrons. Results are presented in connection with a converter-target specific geometry.

**PACS.** 25.85.Ca Spontaneous fission – 25.85.Ec Neutron-induced fission – 24.75.+i General properties of fission

## 1 Introduction

The fission process of heavy nuclei at low energy gives rise to neutron-rich fragments. Exploiting this property, a source of nuclei towards the stability limit can be conceived [1]. A high flux of neutrons able to produce the fission events can be obtained through the deuteron break-up reaction in some suitable converter placed in the vicinity of the fissioning target. The feasibility study of a facility based on the above concept is the main purpose of the PARRNe [2,3] (Production d'Atomes Radioactifs Riches en Neutrons) ongoing project. The fissioning target is made from $^{238}$U. This work is mainly guided by the NuPECC recommendations established in order to investigate the main options for second-generation radioactive beam facilities in Europe [4]. Such studies were carried also in ref. [5] using the LAHET code in order to estimate fission rates.

In the following, a theoretical optimization of such a combination is elaborated by taking into account the influence of the incident deuteron energy on the variation of the fission isotopic product yields. The $\beta$-decay of unstable isotopes is not considered here. Throughout the rest of this paper, the term fission fragment refers to the fragments before prompt neutron emission, and the term fission products refers to the products after prompt neutron emission [6]. The fission model, initially reported in ref. [7], is presented here in an extended version suitable for symmetric decays. The isotopic distribution for all the fission products can now be determined.

[a] e-mail: mirea@ifin.nipne.ro

The incident energy of the deuteron causes changes in the angular and energetic neutron distributions. So, the converter-target geometry of the facility must be investigated at each incident deuteron energy. The energy of the neutron impinging on the $^{238}$U-target rules the excitation of the compound nucleus $^{239}$U or the residual $^{238}$U obtained in inelastic collisions. It is known that the excitation energy affects the isotopic products yields because the fission barrier is modified for each fragments binary partition $(A_1Z_1, A_2Z_2)$ and the number of evaporated neutrons varies.

The paper begins with a theoretical investigation of the relative variations of the isotopic yields of fission products as a function of the excitation energy of the compound nucleus $^{239}$U and the excited $^{238}$U. The fission model will be presented in the following section. Furthermore, for a given experimental geometry, the yields of the neutron-rich isotopes obtained in the fissioning target are determined with respect to the incident energy of the deuteron. The number of fission events produced in the target for a given converter-target geometry as a function of the incident deuteron energy will be deduced. Results are commented in connection with experimental data in the last section.

## 2 Fission model

This neutron-induced fission model is based essentially on the hypothesis of a sudden dissipation process of the excitation energy carried in by the incident neutron.

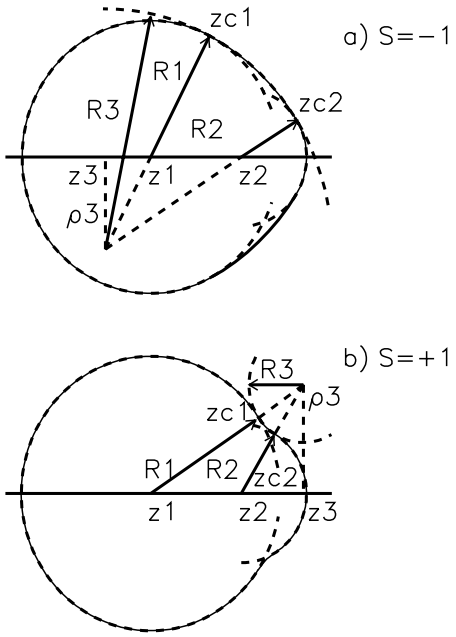


**Fig. 1.** The nuclear shape parametrization. The upper part corresponds to a negative neck parameter $C = S/R_3$, while the lower one corresponds to positive $C$ values.

### 2.1 Nuclear shape parametrization

Due to the leptodermous character of the nuclear systems, it is convenient to consider that during the fission, the shape degrees of freedom vary and rule the evolution of the system. In general, many degrees of freedom are needed to specify accurately the shape of a decaying nucleus. It is however considered that a set of three degrees of freedom is the barest minimum to display the essential features of fission: the elongation, the necking and the mass asymmetry [8].

The nuclear parametrization is defined by joining smoothly two intersecting spheres of radius $R_1$ and $R_2$ with a neck surface generated by the rotation of a circle of radius $R_3$ around the symmetry axis [9], as presented in fig. 1. The distance between the center of this circle and the axis of the symmetry is given by $\rho_3$. By imposing the condition of volume conservation, the surface is perfectly determined by the values of the parameters $R$ (distance between the centers of the spheres), $R_3$ (the radius of the neck) or $C = S/R_3$ (where $S = +1$, when $\rho_3 - R_3 \geq 0$ and $S = -1$, when $\rho_3 - R_3 < 0$) and $R_2$ (the radius of the emitted fragment) or $\eta = \frac{V_1 - V_2}{V_0}$. These three parameters characterize the elongation, the necking and the mass asymmetry, respectively. Due to the axial symmetry of this system, the surface equation is given in cylindrical coordinates

$$\rho_s(z) = \begin{cases} \left[R_1^2 - (z - z_1)^2\right]^{1/2}, & z \leq z_{c1}, \\ \rho_3 - S\left[R_3^2 - (z - z_3)^2\right]^{1/2}, & z_{c1} < z < z_{c2}, \\ \left[R_2^2 - (z - z_2)^2\right]^{1/2}, & z \geq z_{c2}. \end{cases} \quad (1)$$

For extremely large values of $R_3$, that means for $C = S/R_3 \approx 0$ fm$^{-1}$ the parametrization in the interval $z_{c1} < z < z_{c2}$ is described by the relation

$$\rho_s(z) = [a(z - z_{c1}) + b]^{1/2}$$

with

$$a = \{[R_2^2 - (z_{c2} - z_2)^2]^{\frac{1}{2}} - [R_1^2 - (z_{c1} - z_1)^2]^{\frac{1}{2}}\}/(z_{c2} - z_{c1}),$$

$$b = [R_1^2 - (z_{c1} - z_1)^2]^{\frac{1}{2}}.$$

The significances of all the geometrical symbols are presented by means of fig. 1. Throughout this paper, the subscripts 0, 1 and 2 help to assign the parent, the daughter (heavy fragment) and the emitted (light fragment) nuclei, respectively. The initial radius of the parent is $R_0 = r_0 A_0^{1/3}$, the final radii of the two fragments are $R_{if} = r_0 A_i^{1/3}$, with $i = 1, 2$ and the constant radius $r_0 = 1.16$ fm. In eq. (1), $\rho_s$ denotes the value of the coordinate $\rho$ on the nuclear surface. "Diamond"-like shapes are obtained for $S = -1$ and necked-in shapes for $S = +1$.

When $S = -1$, the volume of the emitted fragment $V_2$ cannot be determined unambiguously without introducing a supplementary hypothesis. In this special case, the shape does not show a separation plane between the nascent fragments. So, it is considered that $V_2$ must be computed from half the distance between the centers $z_2 - R/2$ up to the side $z_2 + R_2$. In the case $S = +1$ we compute this volume between $[z_3, z_2 + R_2]$. When $R_3 = 0$ fm, the simple parametrization of two intersecting spheres is obtained. This nucleus shape parametrization was widely used in nuclear dynamic calculations [10–12] in a large range of mass asymmetries because it accounts for the most important degrees of freedom encountered in fission processes: elongation, necking and mass asymmetry. In the following, sometimes, in place of $R$ we use $R/\Delta$ which defines the normalized coordinate of elongation with $\Delta = R_1 + R_2 + 2R_3$ being the point of scission. Also, $\Delta_t = R_{1f} + R_{2f}$ denotes the touching point configuration when the two fragments have spherical shapes.

Instead, the mass asymmetry generalized coordinate $R_{2f}$ used in ref. [7], that is, the final radius of the light fragment, in the following, the quantity $\eta = \frac{A_1 - A_2}{A_0} = \frac{V_1 - V_2}{V_0}$ will be taken as the mass asymmetry. The equation of volume conservation is solved in order to obtain $R_1$ and $R_2$, the radii of the heavy and the light fragment, such that the volumes $V_1$ and $V_2$ correspond to the masses $A_1$ and $A_2$.

In fig. 2, the possible shapes for the symmetric fission of $^{238}$U are plotted with respect to the elongation and the necking of the nuclear system. For positive values of the parameter $C = S/R_3$ we obtain necked shapes, while, for negative values of C, the parametrization gives swollen shapes in the central region. Swollen shapes are geometrically possibles only up to a fixed value of the elongation, depending on $C$. In the positive region, the elongation for the scission configuration decreases with increasing $C$, reaching the lower limit $\Delta_t = r_0(A_1^{1/3} + A_2^{1/3})$ for $R_3 = 0$ fm.

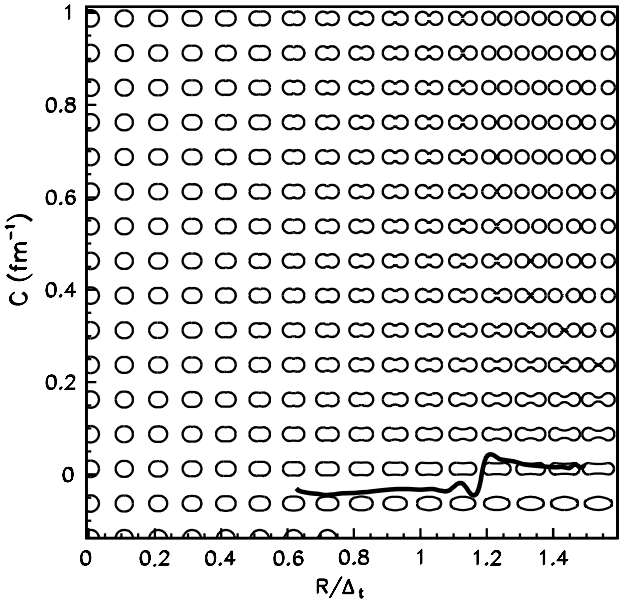


**Fig. 2.** Family of nuclear shapes in the $(C, R/\Delta_t)$ plane for the symmetric fission of $^{238}$U. $\Delta_t = r_0(A_1^{1/3} + A_2^{1/3})$ is the elongation which characterizes the two tangent spheres configuration. The path obtained by minimizing the integral action is plotted with a thick line.

## 2.2 Penetrabilities

The probability to obtain a binary partition $(A_H Z_H, A_L Z_L)$ is ruled by the barrier penetrability. Using the last action trajectory principle it is possible to obtain the path in the configuration space followed by the fissioning system [13]. The quantum penetrability

$$P = \exp\left\{-\frac{2}{\hbar}\int_{R_i}^{R_f}\sqrt{2B\left(q_i, R, \frac{\partial q_i}{\partial R}\right)[E_d(q_i,R) - E_v]}\mathrm{d}R\right\} \quad (2)$$

is calculated by using the semi-classical Wentzel-Kramers-Brillouin (WKB) approximation. The region of interest is classically forbidden. However, the action trajectory is determined along a classical trajectory between the initial $R_i$ and final $R_f$ turning points corresponding to the entrance into the sub-barrier region and the exit on the other side of the potential. The two turning points are fixed by the same value of the deformation energy, that is, $E_d(q_i, R_i) = E_d(q_i, R_f) = E_v$. Here, $\{q_i\}$ denotes the set of generalized deformation parameters, excepting the elongation $R$. In the functional (2), $B$ gives the inertial mass, $E_d$ is the deformation energy determined so that its value in the ground state is zero and $E_v \approx 0.5$ MeV is the zero-point vibration energy. The condition of consistence must be fulfilled: the same shape for the inertia, the microscopic and macroscopic energies.

## 2.3 Deformation energy

The main key steps to deduce the deformation energy $E_d$ are presented in the following.

### 2.3.1 Macroscopic deformation energy

The macroscopic deformation energy was computed in the framework of the Yukawa-plus-exponential [14] model extended for binary systems with different charge densities [15], where another degree of freedom is introduced, namely, the charge asymmetry. The charge density of the system is kept initially unchanged (up to $0.7\Delta_t$), and in the final stages of the process, where very necked forms are reached, the charge densities of the two fragments are linearly varying functions of $R$ up to their final values in the output channel. The values of the numerical parameters are from ref. [16]. Both nuclear $E_n$,

$$E_n = -\frac{a_2}{8\pi^2 r_0^2 a^4}\int_V\int_V\left(\frac{r_{12}}{a} - 2\right)\frac{\exp(-\frac{r_{12}}{a})}{\frac{r_{12}}{a}}\mathrm{d}^3r_1\mathrm{d}^3r_2 \quad (3)$$

and Coulomb $E_c$,

$$E_c = \frac{1}{2}\int_\infty\int_\infty\frac{\rho_e(\mathbf{r_1})\rho_e(\mathbf{r_2})}{r_{12}}\mathrm{d}^3r_1\mathrm{d}^3r_2 \quad (4)$$

(with $r_{12} = \mid \mathbf{r_1} - \mathbf{r_2} \mid$) energies are expressed as a sum of three shape dependent terms: the self-energies of the fragments ($B_{ni}$, $B_{ci}$, $i = 1, 2$), plus the interaction energy ($B_{n12}$, $B_{c12}$)

$$E_n/E_n^0 = (c_{s1}/c_s)B_{n1} + [(c_{s1}c_{s2})^{1/2}/c_s]B_{n12} + (c_{s2}/c_s)B_{n2} \quad (5)$$

$$E_c/E_c^0 = (\rho_{1e}/\rho_{0e})^2 B_{c1} + (\rho_{1e}\rho_{2e}/\rho_{0e}^2)B_{c12} + (\rho_{2e}/\rho_{0e})^2 B_{c2}, \quad (6)$$

where $E_n^0$ and $E_c^0$ correspond to the spherical shapes, $\rho_{ie}$ are charge densities and

$$c_{si} = a_s[1 - \kappa_s(N_i - Z_i)^2/A_i^2], \quad (7)$$

$$\rho_{ie} = 3eZ_i/(4\pi r_0^3 A_i) \quad (8)$$

with the parameters: $a_s = 21.13$ MeV, $\kappa_s = 2.3$, $a = 0.68$ fm, $a_V = 15.9937$ MeV, $\kappa_V = 1.927$. The quantities $B_{ni}$ and $B_{ci}$ in the above equations are dependent on the nuclear shape; their expressions containing two- and threefold integrals are evaluated by numerical quadrature.

Furthermore, the contribution of the volume energy $E_V$ is added proportionally to the light fragment radius so that $E_V = 0$ when $R_2 = R_0$ and

$$E_V = E_{V1} + E_{V2} - E_{V0} \quad (9)$$

when $R_2 = R_{2f}$. The volume self-energies of the fragments are

$$E_{Vi} = -a_V[1 - \kappa_V(N_i - Z_i)^2/A_i^2]. \quad (10)$$

A linear interpolation also proportional to the light volume fragment is used to simulate the existence of the Wigner energy $E_\mathrm{W}$

$$E_{\mathrm{W}i} = -7\exp(-6 \mid I_i \mid) \quad \mathrm{MeV}, \quad (11)$$

where $I_i = (N_i - Z_i)/A_i$ is the relative neutron excess of each nucleus.

So, the total deformation macroscopic energy becomes

$$E_{\rm LDM} = E_n + E_c + (E_V + E_{\rm W})\frac{R_2 - R_0}{R_{2f} - R_0} - E_0, \quad (12)$$

where $R_2$ is the radius of the light fragment during the fission process (it begins from $R_0$ for the initial parent considered spherically and reaches its final radius $R_{2f}$ after the scission). $E_0$ is the liquid drop energy of the spherically parent.

In the barrier region, the modulation of the potential energy surface by shell effects leads to the famous double-humped barrier for actinides. These effects are based on the following microscopic treatment.

### 2.3.2 Level scheme

The single-particle energetic levels are obtained with an improved version of the Superasymmetric Two-Center Shell Model (STCSM) inspired from the work of Maruhn and Greiner [17]. For a rigorous analysis of the microscopic model, the reader can refer to ref. [18] and refs. [19,20], where the model was improved. The STCSM was proved a useful tool in the microscopic treatment of superasymmetric fission, including cluster [19–21] and alpha [22] decay.

For the nuclear shape parametrization presented above, the microscopic potential (in cylindrical coordinates) is split into several parts which are treated separately

$$V(\rho, z, \varphi) = V_0(\rho, z) + V_{as}(\rho, z) + V_n(\rho, z) + V_{ls}(\rho, z, \varphi) + V_{l^2}(\rho, z, \varphi) - V_c, \quad (13)$$

where $V_0(\rho, z)$ represents the two-center harmonic potential whose eigenvectors can be analytically obtained by solving the Schrödinger's equation. It is given by the relation

$$V_0(\rho, z) = \begin{cases} \frac{1}{2}m_0\omega_{z1}^2(z + z_1)^2 + \frac{1}{2}m_0\omega_\rho^2\rho^2, & z < 0 \\ \frac{1}{2}m_0\omega_{z2}^2(z - z_2)^2 + \frac{1}{2}m_0\omega_\rho^2\rho^2, & z \geq 0, \end{cases} \quad (14)$$

where $m_0$ is the nucleon mass, $z_1$, $z_2$ (reals, positives) represent the distances (conditioned by the relation $z_1 + z_2 = R$) between the centers of the two spherical fragments and the intersection plane between the spherical shape of the daughter and the spheroid shape which overlaps the emitted nucleus (see fig. 2 in ref. [18]), and $\omega_i$ are the oscillator stiffnesses. In the case of symmetric fragmentation, $\omega_{z1} = \omega_{z2} = \omega_\rho$ and the parity becomes a good quantum number. The eigenvalues and the eigenvectors for reflection symmetric systems must be deduced using the mathematical formalism presented in refs. [23, 24].

The role played by the other terms in the total potential, *i.e.*, $V_{as}$, $V_n$, $V_{ls}$, $V_{l^2}$, $V_c$ is related to the mass asymmetry, to the necking, to the spin-orbit coupling, to the $l^2$ correction and to the depth of the potential, respectively and are defined as in ref. [18].

Due to the cylindric symmetry of the system, the quantum numbers along the $\rho$-axis ($n_\rho$) and $\varphi$-coordinates ($m$) are constants of the motion. This property leads us to know which adiabatic levels are occupied by an unpaired nucleon during the process as a function of the final splitting of the system. In these circumstances, we are able to apply the blocking effect to the unpaired nucleons during the fission process for each studied channel.

The spin orbit and $l^2$ coefficients are obtained from ref. [25] by interpolating the published values as a function of their mass. $V_c$ is considered 0. These coefficients are mainly determined for nuclei close to the stability line. Therefore, we do not expect very accurate results in the mass determination of neutron-rich isotopes.

### 2.3.3 Shell effects

The shell effects are computed using the well-known Strutinsky procedure [13,26]. The total energy is the sum of the liquid drop energy and the shell and pairing effects due to the proton and neutron level schemes.

The shell correction is

$$\delta V_{p(n)} = \Big[\sum_{\nu=1}^{Z(N)} \epsilon_\nu - \int_{-\infty}^{\tilde{\lambda}} \epsilon\tilde{g}(\epsilon)\ \mathrm{d}\epsilon\Big], \quad (15)$$

where $\epsilon_\nu$ are the single-particle energies, $\tilde{\lambda}$ is the Fermi energy for the smoothed level density,

$$\tilde{g}(\epsilon) = \frac{1}{\tilde{\gamma}}\int_{-\infty}^{\infty} \mathcal{F}(\frac{\epsilon - \epsilon'}{\tilde{\gamma}}) \sum_\nu \delta(\epsilon - \epsilon_\nu)\mathrm{d}\epsilon' \quad (16)$$

is the mean density of single-particle levels, $\tilde{\gamma}$ is an interval around the Fermi energy which is taken at least 1.15 (in $\hbar\omega$ units) times the value of the mean distance between the major shells of the light fragment, while

$$\mathcal{F}(x) = \frac{1}{\pi^{1/2}}\exp(-x^2)\sum_{k=0,2}^{2m} a_k H_k(x^2)$$

is the well-known Strutinsky smoothing function with Hermite polynomials. The single-particle levels are normalized with $\hbar\omega$. As remarked in ref. [27] for asymmetric fission processes, the shell effects are determined more accurately if $\hbar\omega$ has the value associated with the mass of the light fragment. So, it is considered that $\hbar\omega$ varies linearly from $\hbar\omega_0 = 41/A_0^{1/3}$ to $\hbar\omega_2 = 41/A_2^{1/3}$ at scission, in a way similar to that mentioned for the charge asymmetry. For the same reason, in the present calculations $\tilde{\gamma} = 1.4$. The sum over $\nu$ means for all the levels with energies below the last occupied level. The smooth value of the Fermi energy $\tilde{\lambda}$ is obtained as usual from the condition of number conservation. If the parent possesses an odd number of protons ($Z$) or neutrons ($N$), the procedure is the same, taking care to consider the last level nondegenerate in the sum (15) and in the particle number conservation equation. If the nucleus is excited, the pair initially located

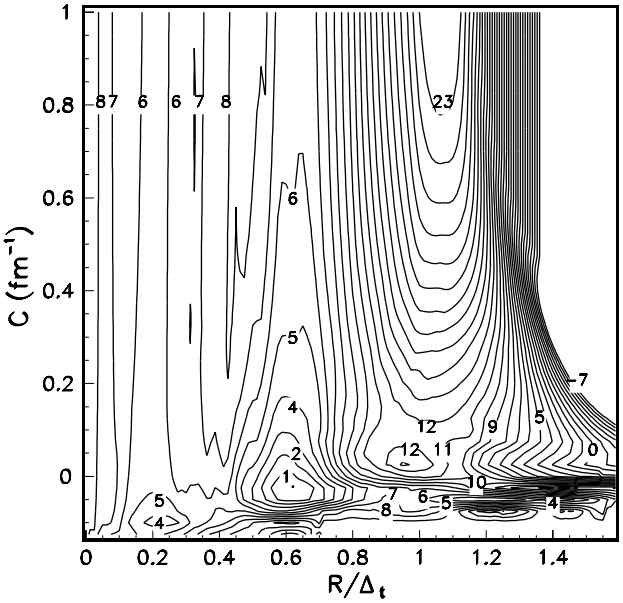


**Fig. 3.** The $^{238}$U deformation energy $E_d$ in MeV for symmetric nuclear shapes. The step value between the equipotential lines is 1 MeV. Some values of the energies are marked on the plot. The ground state is located by a point of coordinates $R/\Delta_t = 0.62$ and $C = -0.022$ fm$^{-1}$.

in the last occupied level $\epsilon_0$ is broken and two unpaired nucleons reach the levels $\epsilon_1$ and $\epsilon_2$. Consequently, a correction $C_{\rm cor} = |\epsilon_1 - \epsilon_0| + |\epsilon_2 - \epsilon_0|$ is added to the shell effects.

The pairing correction is (for protons label $p$ and for neutrons label $n$)

$$\delta P_{p(n)} = P - \frac{1}{2} g(\tilde{\lambda}) \tilde{\Delta}^2, \tag{17}$$

where $P$ is the pairing value obtained directly from the level scheme, while $\tilde{\Delta} = 12/A^{1/2}$ is the smoothed distribution gap parameter. $\Delta$ and $\lambda$ are deduced from the BCS equations on the form

$$\sum_{\nu=n-n_c}^{n+n_c} \frac{1}{[(\epsilon_\nu - \lambda)^2 + \Delta^2]^{1/2}} = 2\tilde{g}(\tilde{\lambda}) \ln\left(\frac{2\Omega}{\tilde{\Delta}}\right), \tag{18}$$

$$Z(N) = \sum_{\nu} 1 - \frac{\epsilon_\nu - \lambda}{[(\epsilon_\nu - \lambda)^2 + \Delta^2]^{1/2}} \tag{19}$$

and $\Omega$ is an energetic interval of the order of $\tilde{\gamma}$, $2\Omega = 2n_c/\tilde{g}(\tilde{\lambda})$ is the number of states taken into account. The phenomenological gap parameter $\tilde{\Delta}$ was forced to vary linearly from $12/A_0^{1/2}$ up to $12/(A_1^{1/4} A_2^{1/4})$ as considered for the charge asymmetry. For odd filled level we appealed to the blocking effect in computing this correction.

The deformation energy

$$E_d = E_{\rm LDM} + \delta V_p + \delta V_n + \delta P_p + \delta P_n \tag{20}$$

in MeV is represented in fig. 3 for the symmetric fission of $^{238}$U. In this representation, the energy reference was modified such that $E_d = 0$ in the ground-state position. This plot evidences a very pronounced minimum which belongs to the ground state, marked with a point. A second minimum, at 4 MeV, is located at a more elongated shape and smaller values of $C$. The calculations presented in fig. 3 are achieved under the assumption that the energy levels are filled pairwise.

### 2.4 Excitation energy

The excitation energy brought by the incident neutron modifies the potential barrier and the ground-state energy. It is considered that a preformation of the fission channel occurs when the target nucleus receives energy. For example, in the case of protons, the excitation energy can break a pair of protons and the atomic numbers of the nascent fragments $Z_1$ and $Z_2$ become odd. In this early stage, two single-particle levels, $\epsilon_H$ and $\epsilon_L$ belonging to the heavy and light fragments will be occupied by unpaired protons. As briefly mentioned above, the deformation energy for odd $Z_1$ and $Z_2$ must be corrected and must be now determined using the relation $\delta V_p^{\rm odd} = \delta V_p + |\epsilon_H - \epsilon_0| + |\epsilon_L - \epsilon_0|$. It must be pointed out that the pairing correction takes into account the blocking of the levels $\epsilon_H$ and $\epsilon_L$. The excitation energy will be $E^* = E_c^* - |\epsilon_H - \epsilon_0| - |\epsilon_L - \epsilon_0|$, where $E_c^*$ is the initial energy brought by the neutron. In this particular case, if $E^* < 0$, the barrier is increased with $|E^*|$.

We use the Franck-Condon principle in a sense similar to that presented in ref. [28] where it is evidenced that, in an ideal collective model, the excitation process takes place in such a way that the positions and velocities coordinates of the heavy part of the system remain unchanged. For a fixed point in the configuration space of the deformation coordinates, associated to the ground state of the system, we assume the system shifts from one potential to another. In our interpretation, this principle is equivalent to say that the "damping", as one way to speak of the exchange between vibration and nucleonic excitation, is produced in a very short time at the beginning of the process. So, this model is based on a sudden dissipation process.

The excitation energy will damp the shell effects. For simplicity, we assume an exponential decay [29]

$$U_{\rm tot} = E_{\rm LDM} + \delta U(T=0) \exp(-T^2/T_0^2), \tag{21}$$

where $E_{\rm LDM}$ is the liquid drop potential along the trajectory path and $\delta U = \delta V_p + \delta V_n + \delta P_p + \delta P_n$ is the sum of shell and pairing corrections (for both the neutron and proton scheme). The nuclear temperature $T$ is connected with the excitation energy [30]

$$E^* = \frac{1}{9} A_0 T^2 - T, \tag{22}$$

where the value $T_0 = 1.5$ MeV allows the shell corrections to vanish if $E^* > 60$ MeV. So, when the nucleus is excited, according to the Franck-Condon effect, the system will jump from a ground-state potential energy to

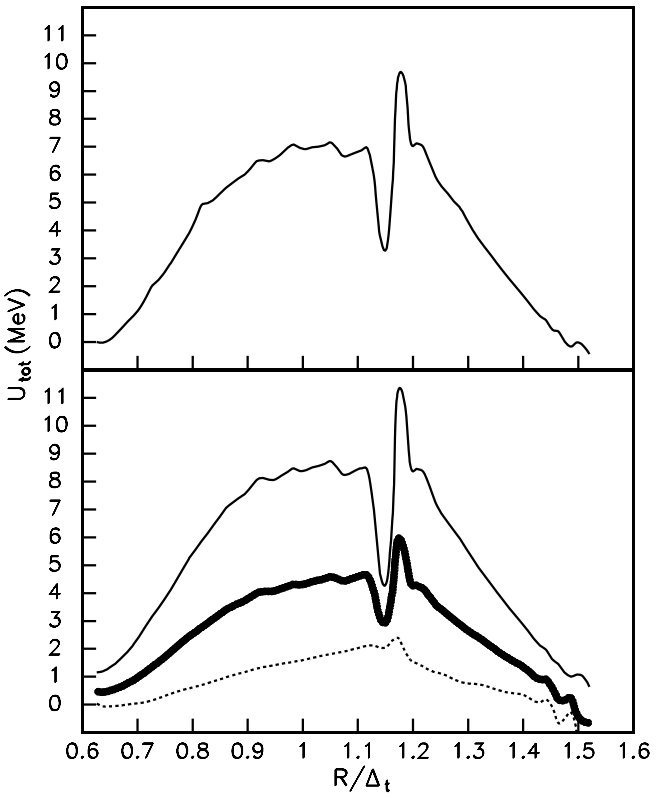


**Fig. 4.** Top: Mass and charge symmetric fission barrier obtained along the path of minimum action integral by considering that the single-particle levels are pairwise filled and $E^* = 0$ MeV. Bottom: Mass and charge symmetric fission barriers calculated at three excitation energies considering that the last neutron pair is broken. The trajectory in the configuration space is the same as in the upper part of the figure. Full line: $E^* = 0$ MeV; dashed line: $E^* = 50$ MeV and dotted line: $E^* = 200$ MeV. Due to the Franck-Condon effect, the system shifts from the potential barrier at $E^* = 0$ MeV to another one.

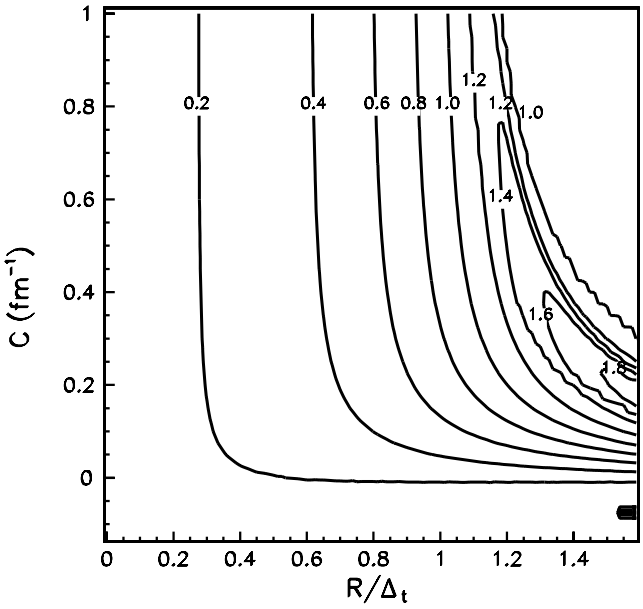


**Fig. 5.** The $^{238}$U $B_{RR}/\mu$ diagonal element of the inertia tensor for symmetric nuclear shapes. $\mu = A_1A_2/A_0$ is the reduced mass of the system. The difference between two contour level values is 0.2.

another, characterized by a fixed nuclear temperature. The deformation energy at a temperature $T$ will be now $E_d(T) = U_{\rm tot}(T) - U^{\rm gs}_{\rm tot}(T)$, where $U^{\rm gs}_{\rm tot}(T)$ is the deformation energy at the same temperature $T$ in the ground-state point of the configuration space at $T = 0$.

In fig. 4, the Franck-Condon principle is illustrated for the mass and charge symmetric $^{238}$U fission. In the present formalism, the Franck-Condon principle is employed during the whole fission process, beginning with the ground-state nuclear shape. This principle allows a determination of the deformation energy shift produced by the rupture of a nucleon pair and due to the excitation energy. Otherwise, the ground-state energy is not modified. The energy shift, produced by a nucleon pair rupture, is also subject to the exponential law (21). So, at high energies, this energy shift vanishes, in a similar manner as the shell effects. Nevertheless, this treatment can produce a very large odd-even effect in the fragment yield distributions, especially at low energies.

It must be mentioned that the STCSM only simulates the variation of the single-particle levels towards swollen nuclear shapes in the central region, that is, for small values of $C$. In other words, the model is not adequate to obtain good positions of the single-particle energies in the region of small values of $C$ because the spin orbit and $L^2$ terms are constructed for a two-intersected-spheres parametrization. For example, the definition of the angular momentum $\mathbf{L}$ operator is $\mathbf{L} = \nabla V \times \mathbf{p}$, where $V$ is the deformed single-particle potential. The STCSM uses the two-center potential of two intersected spheres to simulate $V$ in the definition of $\mathbf{L}$. So, the experimental values of the heights of the humped barrier cannot be reproduced exactly.

### 2.5 Tensor of inertia

In a $n$-dimensional deformation space, where the nuclear shape is described by a set of independent coordinates $\{q_i\}$, the inertia tensor $\{B_{ij}\}$ is defined by the equation of kinetic energy $E_k$ [31,32]

$$E_k = \frac{1}{2}\sum_{i,j=1}^{n} B_{ij}(q_1, q_2, ..., q_n)\frac{\partial q_i}{\partial t}\frac{\partial q_j}{\partial t}. \qquad (23)$$

There are different methods of calculation for these quantities. One of the most used methods to obtain the effective mass is the Werner-Wheeler approximation. It is assumed that this tensor is a measure of the collective motion of the nuclear matter. The flow of the fluid is idealized as nonrotational, nonviscous and hydrodynamical. To obtain the inertia $B(s)$ along the trajectory, the multidimensional problem can be reduced to a single-dimensional one

$$B(s) = \sum_{i,j=1}^{n} B_{ij}(q_1, q_2, ..., q_n)\frac{\partial q_i}{\partial s}\frac{\partial q_j}{\partial s} \qquad (24)$$

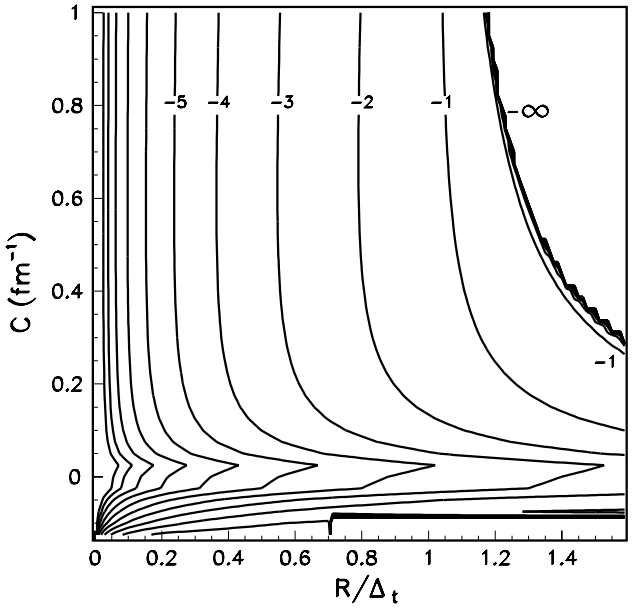


**Fig. 6.** Same as fig. 4 for the $\log_{10}(B_{CC}/\mu)$ diagonal element of the inertia tensor. The dimension of $B_{CC}/\mu$ is fm$^{-4}$. $\mu = A_1A_2/A_0$ is the reduced mass of the system. The difference between two contour level values is 1.

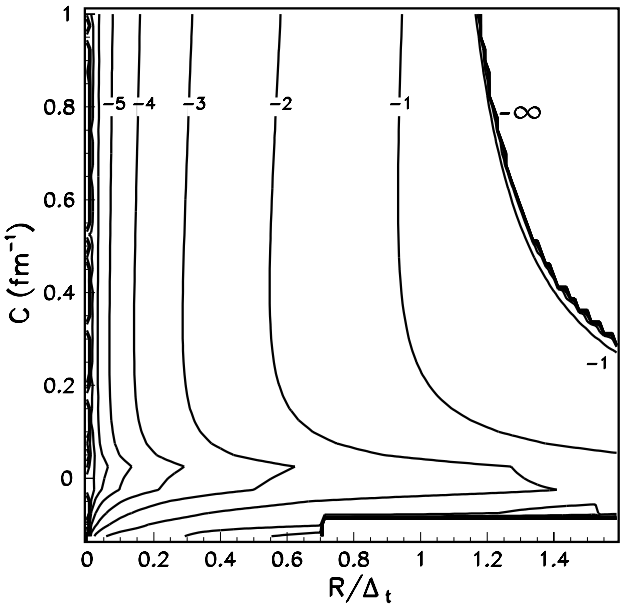


**Fig. 7.** Same as fig. 4 for the $\log_{10}(B_{RC}/\mu)$ off-diagonal element of the inertia tensor. The dimension of $B_{RC}/\mu$ is fm$^{-2}$. $\mu = A_1A_2/A_0$ is the reduced mass of the system. The difference between two contour level values is 1.

for a path given parametrically by the equations $q_i = q_i(s)$. $s$ is generally an independent, arbitrary parameter, but could be chosen as one of the independent generalized coordinates, in particular $R$, like in our case.

In the case of symmetric decays, the shapes are ruled by two degrees of freedom: the elongation $R$ and the necking $C$. The variations of the diagonal elements $B_{RR}$ and $B_{CC}$, together with those of the off-diagonal $B_{RC} = B_{CR}$ term are plotted in figs. 5, 6 and 7. It is interesting to note that, while the lower values of the deformation energy $E_d$ can be found in the region characterized by small values of $C$, the effective masses increase in this region of the configuration space. Very large values can be obtained in the scission region. After the rupture, $B_{RR} = \mu = A_1A_2/A_0$, *i.e.*, the reduced mass of the system and $B_{CC} = B_{RC} = 0$.

### 2.6 Action integral minimization

It is not practically possible to compute the least-action trajectories for all fragment partitions $(A_1Z_1, A_2Z_2)$ and for all excitation energies $E^*$. Therefore, the least-action trajectory was determined for the symmetric cold fission process of the parent $^{238}$U and it was considered that the parametrical form obtained for this path represent a good approximation for the other channels.

In the case of symmetric decays, the shapes are ruled by two independent degrees of freedom: the elongation and the necking. The action integral is minimized in a bidimensional configuration space. The first turning point $R_i$ of the action integral denotes the ground state of the parent. The second turning point $R_f$ must be on the equipotential line of the exit barrier deformation energy surface fulfilling the condition $E_d(C, R_f) = E_d(C, R_i)$= constant. This condition determines a dependence $R_f = f(C)$. For each $R_f$ a local minimum of the action integral can be found. Using a simple numerical method [33,34] the path, associated to the local minimum, followed by the nuclear system can be parametrized. The action integral functional is approximated with the Gauss-Legendre quadrature, that is, a function which depends on a set of variables $\{C_j\}$ giving the values of the necking-in for different values of the elongations $\{R_j\}, R_j \subset (R_i, R_f)$

$$\int_{R_i}^{R_f} \sqrt{2B\left(R, C, \frac{\partial C}{\partial R}\right) E(R,C)}\mathrm{d}R \approx \sum_{j=1}^{N_g} w_j \sqrt{2B\left(R, C_j, \frac{\partial C}{\partial R}\Big|_{R=R_j}\right) E(R_j, C_j)}(R_f - R_i), \quad (25)$$

where

$$B\left(R, C, \frac{\partial C}{\partial R}\right) = B_{RR} + B_{CC}\left(\frac{\partial C}{\partial R}\right)^2 + 2B_{RC}\frac{\partial C}{\partial R} \quad (26)$$

is the inertia along the trajectory. Here, $w_j$ represents the Gauss-Legendre weights, $R_j$ are the mesh points of the quadrature and, in the present calculations, $N_g = 32$. So, the action integral which was a functional of the path $C(R)$ in the configuration space depends now on an even number of variables $C_j$ fixed in the mesh points. The derivatives $\frac{\partial C}{\partial R}\big|_{R=R_j}$ were obtained using spline interpolations. The global minimum can be found by evaluating the local minimum for all the possible exit point of the barrier $R_f$. The global minimum path evaluated numerically in this manner is presented in fig. 2. As mentioned, because the evaluation of the trajectories for all possible partitions and all the excitation energies is not reasonable in practice, this parametrization of the path will

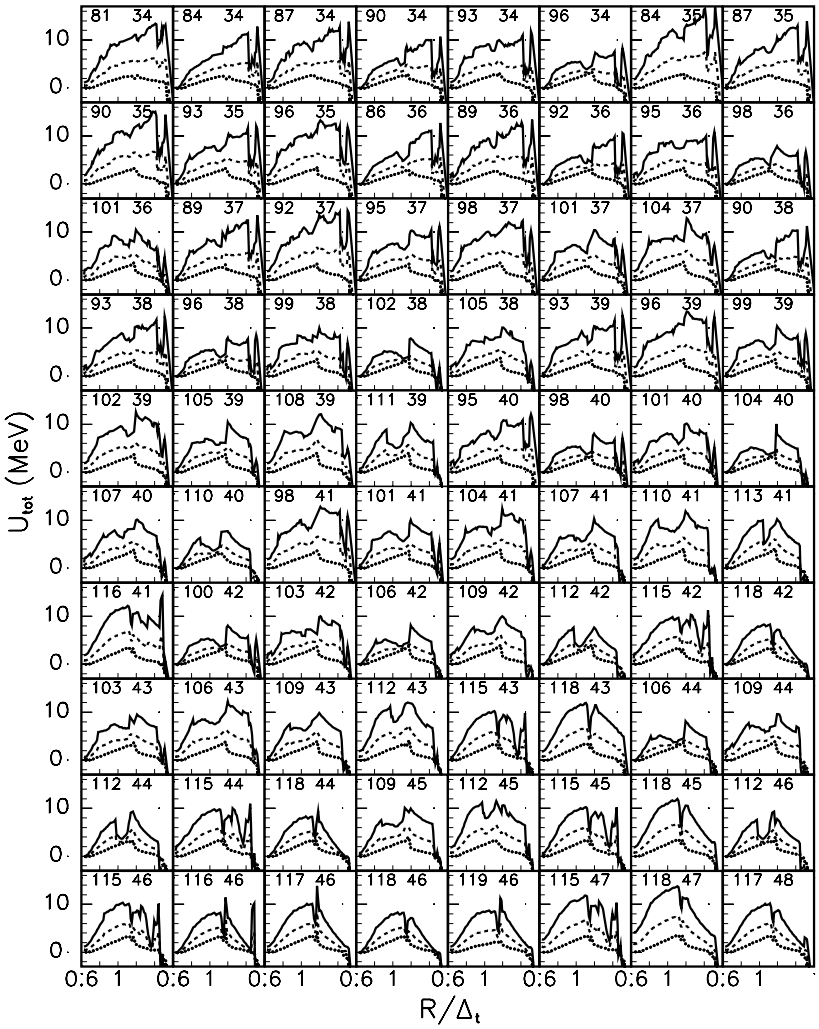


**Fig. 8.** The $^{238}$U fission barriers are represented scanning the entire range in $Z$ while the $N$ range in step of three neutrons. The values of $A_{2f}$ and $Z_{2f}$ are marked on each plot. The full line corresponds to $E^*$= 0 MeV, the dashed line to $E^*$= 50 MeV and the dotted line to $E^*$= 200 MeV.

be extrapolated for all mass asymmetries and any excitations. For asymmetric fission processes, a linear variation of the asymmetry parameter $\eta$ from 0 (in the ground state of the parent) and the final $\frac{A_1-A_2}{A_0}$ (when the scission is reached) is taken into account. This kind of treatment is partially supported by the affirmation found in refs. [35, 36] that the trajectories for spontaneous and induced fission are identical or at least similar. Another argument in favour of this treatment can be extracted in connection with the topographic theorem [37]. This theorem asserts that the saddle point shape of the fission is better determined in the frame of the macroscopic theory, neglecting the shell effects. This statement follows from energetic considerations. Fortunately, our optimum path is determined in the neighbourhood of $C = 0$, in a region where the variations *vs.* $C$ of the macroscopic energies are negligible and where the macroscopic deformations energies reached their lower values. This energetic behavior somewhat justifies our working extrapolation of the fission path at all excitation energies.

The potential barriers obtained in this way are displayed in figs. 8 and 9 for all the asymmetries, the light fragment mass scanning all the interval taken into consideration. A second minimum is clearly visible in almost all the cases at $R/\Delta_t \approx 1.2$. Also, the heights of the two barriers have lower values in the even $A_{2f}$ = 100–106 zone. Between the two turning points (defined $R_i$ and $R_f$ in the text, where $R_f$ is the exit turning point) we used the path parametrization obtained for symmetric fission. But, there are no reasons that the deformation energy in the case of asymmetric channels reaches the value 0 MeV in $R_f$. So, a point with coordinates $C = 0.245$ fm $^{-1}$ and $R/\Delta_t = 1.74$ was added to the parametrization. In this point, the deformation energy is negative for all the channels, that helps us to obtain the second turning point. However, it seems that for very large charge and mass asymmetries, the energy adiabatic exit valley (situated approximatively along a line in fig. 3 from $C \approx 0.025$ fm$^{-1}$, $R/\Delta_t = 1.1$ to 1.6) is shifted towards larger values of $C$, *i.e.*, towards more pronounced necks. The energy island (approximatively

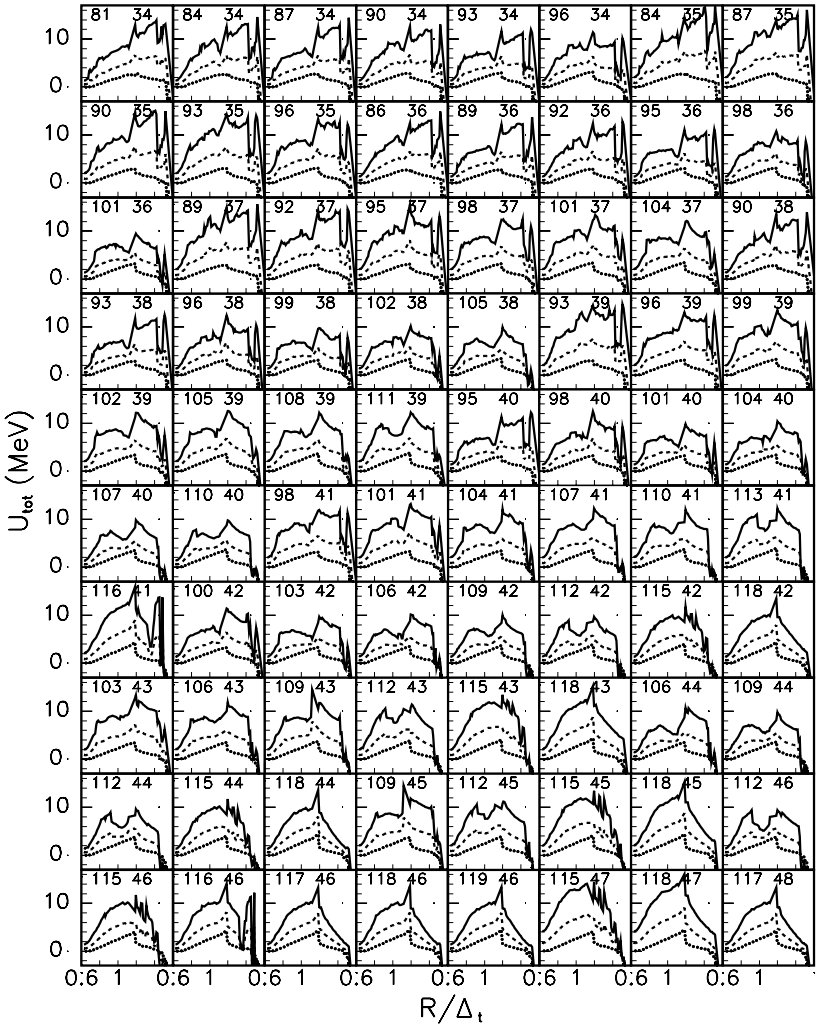


**Fig. 9.** Same as fig. 8 for $^{239}$U fission.

located by the value of 10 MeV in fig. 3 of coordinates $C \approx 0$ and $R/\Delta_t \approx 1.2$) increases with the asymmetries and our path (determined for symmetric fission) penetrates this island in the last point of the infered path parametrization. That behavior produces a thin barrier.

### 2.7 Fragment yields

The fission path being known, it is possible to compute the penetrabilities for each fission fragment partition $(A_1Z_1, A_2Z_2)$. The following simple formula is used for the penetrabilities:

$$P(A_1, Z_1, A_2, Z_2) = \exp\left\{-0.43921\sqrt{\mu}\int_{R_i}^{R_f}\sqrt{E_d - E_v}\,\mathrm{d}R\right\}, \tag{27}$$

where, to avoid cumbersome calculations, the effective mass was considered approximatively equal to the reduced mass. Here, $E_v \approx 0.5$ MeV is the zero-point vibration energy.

Having in mind that the probability to obtain a partition is proportional to its penetrability, it is possible to obtain the yields $y$ normalized to 200% of the fission fragments

$$y(A_1, Z_1, A_2, Z_2) = \frac{P(A_1, Z_1, A_2, Z_2)}{\sum_{N_Z=N_{Z1}}^{N_{Z2}}\sum_{N_A=N_{A1}(N_Z)}^{N_{A2}(N_Z)} P(A_0-N_A, Z_0-N_Z, N_A, N_Z)} \times 100\,, \tag{28}$$

where $Z_0 = 92$ and $A_0 = 238$ or 239. In this application, the penetrabilities were calculated only for the fission products ranging between $N_{Z1} = 34$, $N_{Z2} = 48$, $N_{A1} \approx N_Z$, $N_{A2} \approx 2N_Z$ which gives reasonable values for the penetrabilities.

Up to now, the isotopic distribution of the fragments was obtained as a function of the excitation energy $E^*$ of the parent. The energy of the compound nucleus modifies the potential barrier, that is, the penetrabilities, and the number of prompt neutrons emitted. These two effects modify the distributions of the final products essentially.

In figs. 10 and 11, the fragment yields for $^{238,239}$U are displayed. At $E^* = 200$ MeV, the symmetric fission

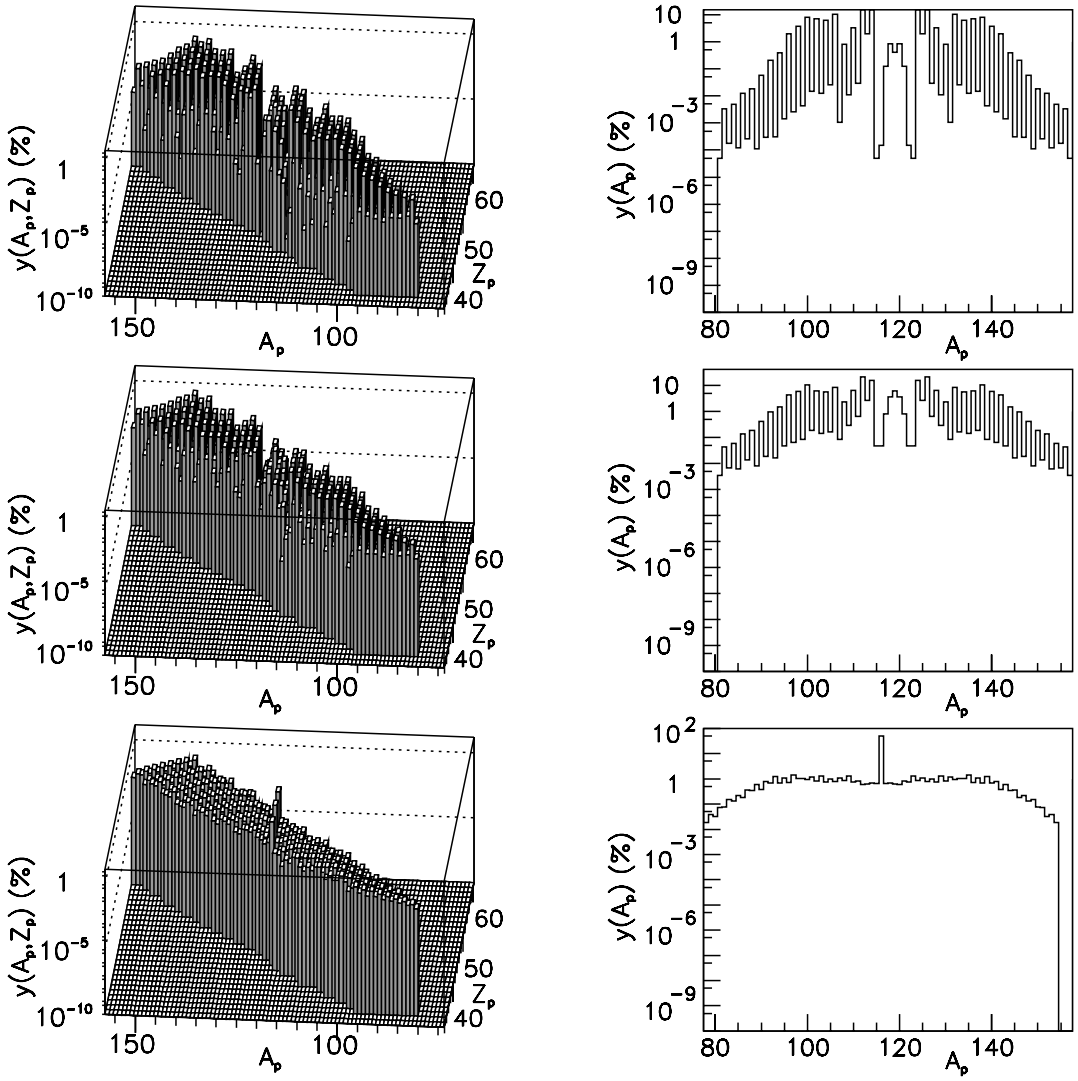


**Fig. 10.** Isotopic and mass fragment yields for three values of the excitation energy (3 MeV top, 50 MeV middle and 200 MeV bottom) for the $^{238}$U-induced fission normalized to 200%.

yield is overestimated. This effect can be explained in the following way. As mentioned in sect. 2.1, in the region of the shapes characterized by $C < 0$, an arbitrary condition is imposed in computing the volume $V_2$. This condition causes a sudden variation of the nuclear shape at large elongations, when the system transits from symmetry to little asymmetries. This change in the nuclear shape parametrization is reflected in an increase of the liquid drop deformation energy for the asymmetric shapes. This variation of the macroscopic barrier is clearly evidenced in fig. 8. Here, the dotted curves (for $E^* = 200$ MeV) for mass symmetry and mass asymmetry fission can be compared.

### 2.8 Neutron evaporation

The fission is accompanied by an almost instantaneous emission of neutrons, which are of decisive importance in calculating the final mass yields. The average number of neutrons emitted per fission is called $\bar{\nu}$. The dependence between the number of emitted neutrons and the excitation energy of the compound nucleus was taken as [38]

$$\Delta(\bar{\nu}(E^*)) = \frac{1}{8.5}E^*. \tag{29}$$

It is also considered that the energy supplied by the incident neutron is shared between the fragments proportionally to their mass. The fragment mass dependence of $\bar{\nu}$ is obtained from the universal neutron yield curves [39]

$$\bar{\nu} \approx 0.08(A_L - 82) + 0.10(A_H - 126), \tag{30}$$

that is

$$\bar{\nu}_H \approx 0.10(A_H - 126), \tag{31}$$

$$\bar{\nu}_L \approx 0.08(A_L - 82), \tag{32}$$

where $\bar{\nu}_H$ and $\bar{\nu}_L$ refer to the evaporated neutrons from the heavy and light fragments, respectively. Here, $A_1 = A_H$

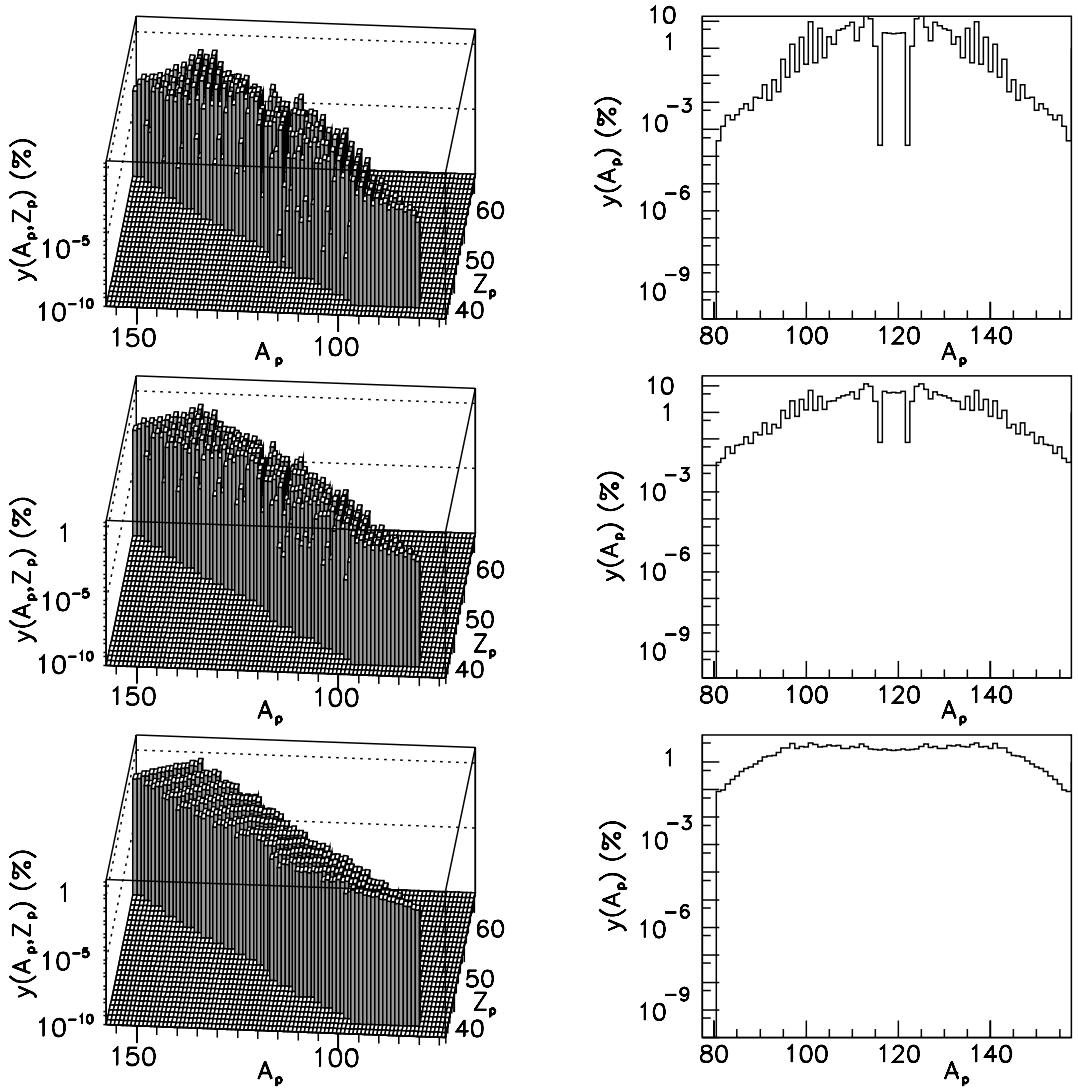


**Fig. 11.** Isotopic and mass fragment yields for three values of the excitation energy (3 MeV top, 50 MeV middle and 200 MeV bottom) for the $^{239}$U-induced fission normalized to 200%.

and $A_2 = A_L$. The distributions of $\bar{\nu}_H$ and $\bar{\nu}_L$ are Gaussian with $\sigma^2 \approx 0.6$. Such a curve rises linearly with mass above $A = 82$ and above 128. In the central range $118 \leq A \leq 128$, the values of $\nu$ were interpolated linearly. The fission product yields $Y(A_1', Z_1')$ and $Y(A_2', Z_2')$ normalized to 200% can be obtained by a folding procedure

$$Y(A_H', Z_1) = \sum_{A_1 = A_H'}^{A_H' + 2\bar{\nu}_H(A_1)} y(A_1 Z_1, A_2 Z_2) \times \frac{\exp\left[-\left(\frac{\bar{\nu}_H - |A_1 - A_H'|}{\sigma}\right)^2\right]}{\sum_{A_H''=A_1-2\bar{\nu}_H(A_1)}^{A_1} \exp\left[-\left(\frac{\bar{\nu}_H - |A_1 - A_H''|}{\sigma}\right)^2\right]}, \quad (33)$$

$$Y(A_L', Z_2) = \sum_{A_2 = A_L'}^{A_L' + 2\bar{\nu}_L(A_2)} y(A_1 Z_1, A_2 Z_2) \times \frac{\exp\left[-\left(\frac{\bar{\nu}_L - |A_2 - A_L'|}{\sigma}\right)^2\right]}{\sum_{A_L''=A_2-2\bar{\nu}_L(A_2)}^{A_2} \exp\left[-\left(\frac{\bar{\nu}_L - |A_2 - A_L''|}{\sigma}\right)^2\right]} \quad (34)$$

The fission product yields obtained in this way depend strongly on the parent excitation energy deposited by the incident neutron.

### 2.9 Distributions of fission products

In fig. 12 are displayed the isotopic and the mass distributions of the $^{238}$U fission for $E^* = 3$ MeV (top), $E^* = 50$ MeV (middle) and $E^* = 200$ MeV (bottom). The gross features of the distributions are reproduced. Mass yields observed in low-energy particle induced fission of actinides are generally characterized by double humped

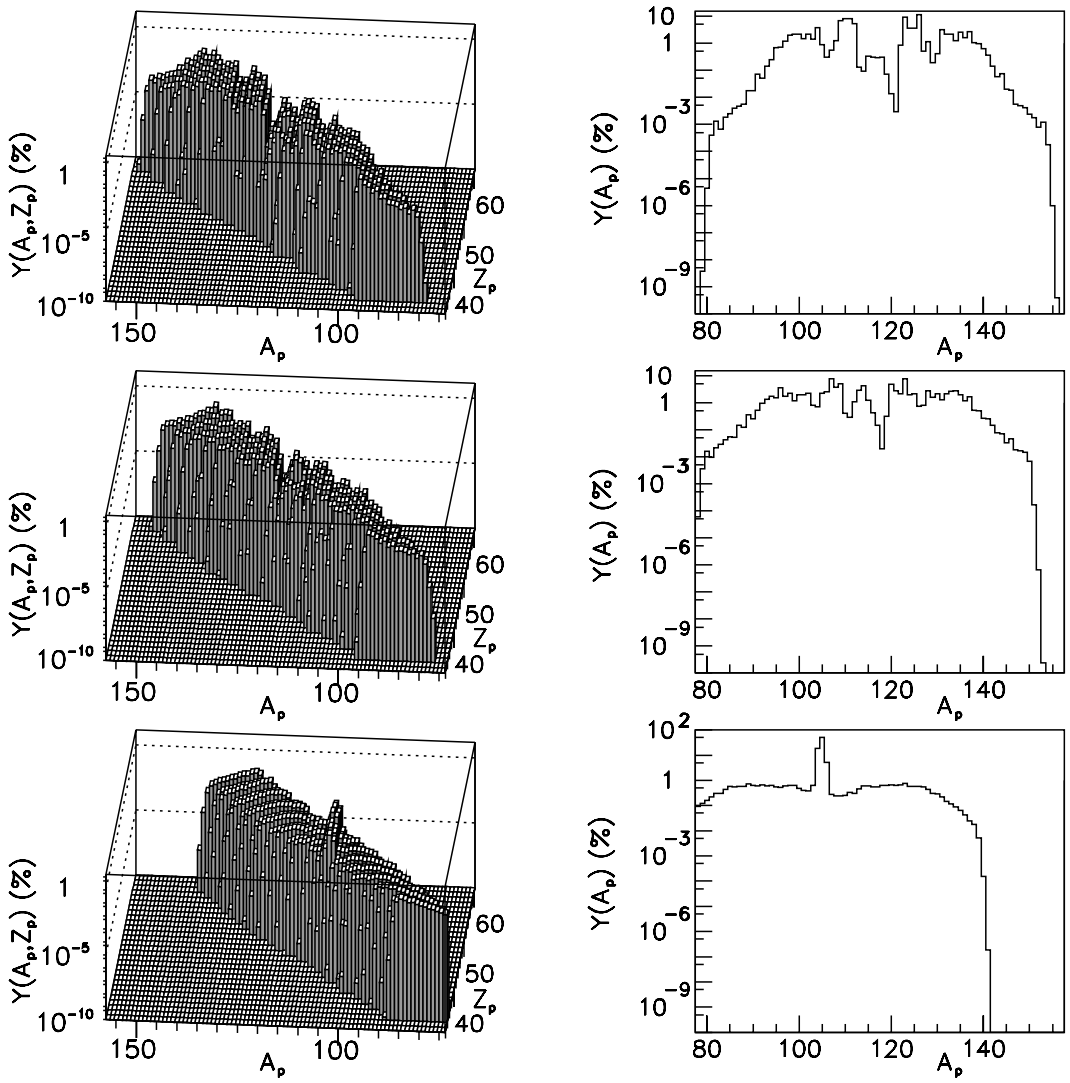


**Fig. 12.** Isotopic and mass products distributions for three values of the excitation energy (3 MeV top, 50 MeV middle and 200 MeV bottom) for the $^{238}$U-induced fission normalized to 200%.

curves showing the preference for asymmetric mass division. The peak to valley ratio reaches several orders in magnitude. In this energy region, the distribution evidences that products with mass 100–110 and 130–140 are widely produced while the symmetric fission process has a lower probability. Increasing the excitation energy, the isotopic distribution becomes broader and the yields towards symmetric fission are enhanced. Also, the maximal values of the yields are shifted towards the stability line, mainly due to the neutron evaporation. The distributions of the $^{239}$U fission are displayed in fig. 13.

The model overestimates the charge odd-even effect. The amplification of this staggering is partially due to the parametrization imposed to the charge density. As mentioned in sect. 2.3.1, the charge densities begin to vary from $0.7\Delta_t$ and reach the final values at scission. As mentioned in ref. [40], it appears that the charges are fixed later, when the neck radius is 1–2 fm. As it can be noticed in fig. 2, a neck radius of 1–2 fm is obtained after the exit point of the barrier, during the so-called rupture. Therefore, during the penetration of the barrier, some experimental information indicate that the nucleus possesses a uniform charge density. In the model, in order to discriminate between different channels, the charge asymmetry was forced to vary during the penetration of the barrier. This observation can be understood in the following way. If $Z_1$ and $Z_2$ are odd numbers, changing the charge densities of our two nascent fragments, the proton single-particle level scheme remains almost unchanged because it depends mainly on the shape coordinates. In the same time, the number of protons $Z_1$, filling the levels of the heavy fragment, can increase (or decrease) while $Z_2$ decreases (or increases). This effect unbalances the last occupied proton single-particle states of the nascent fragments, that is, the difference $C_{\rm cor} = |\epsilon_1 - \epsilon_0| + |\epsilon_2 - \epsilon_0|$ (defined in sect. 2.3.3) increases. Another cause for this large odd-even effect is also due to our hypothesis employed in sect. 2.4 which assesses that a preformation of

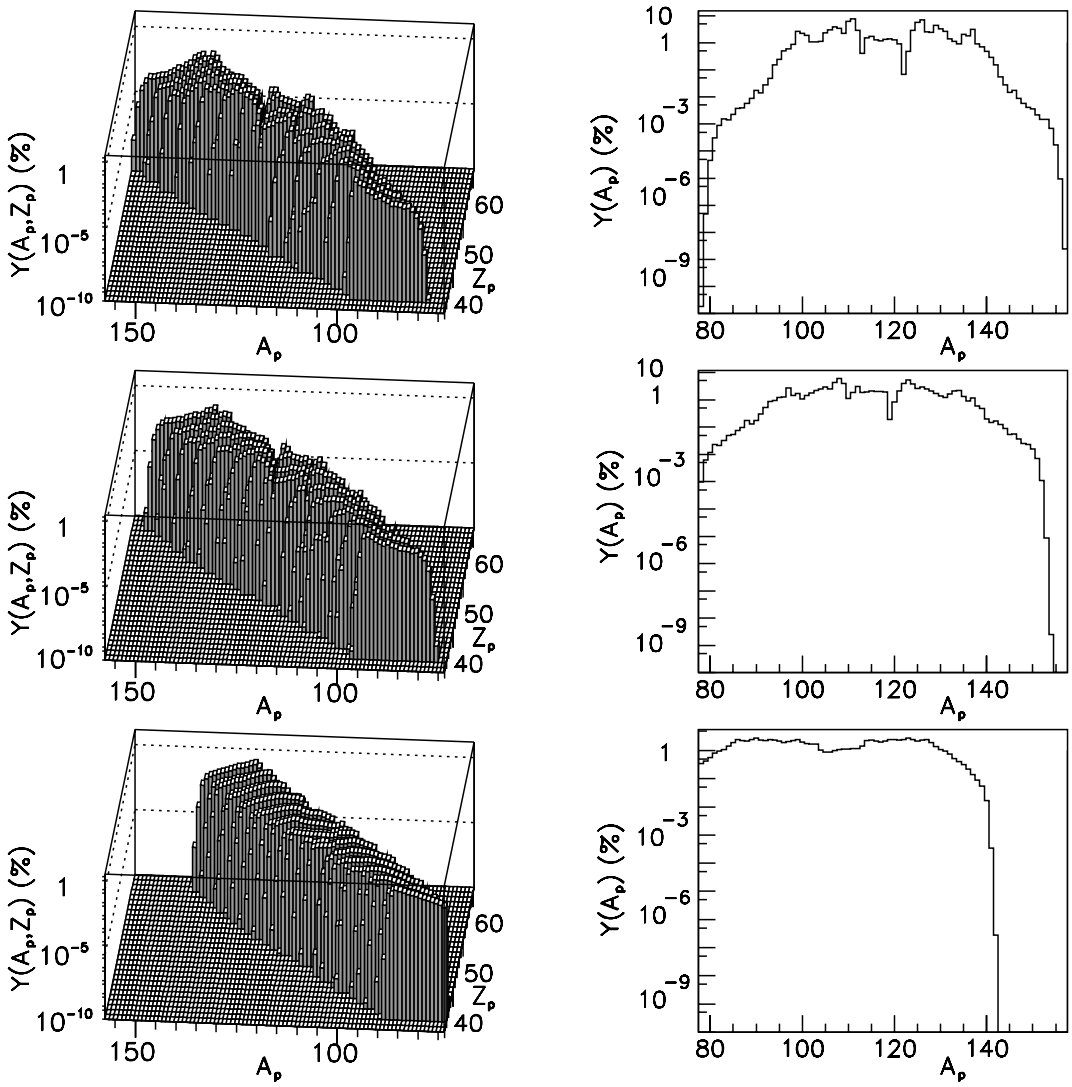


**Fig. 13.** Isotopic and mass products distributions for three values of the excitation energy (3 MeV top, 50 MeV middle and 200 MeV bottom) for the $^{239}$U-induced fission normalized to 200%.

the fission channel occurs when the target nucleus receives energy. That means, a pair is broken at the beginning of the fission process. Therefore, due to the Franck-Condon principle, the barrier is increased. However, this amplification of the odd-even effect is not dramatic because we are mainly interested in the trends exhibited by the product yields as a function of the incident neutron energy, and not by the absolute values of these yields. The variations of the product yields *vs.* the excitation energy of the parent lead us to estimate the optimum parameters for our neutron-rich nuclei source.

The available data concerning the individual products distributions [1] has only three incident neutron energies (thermal, fast and high) and the uncertainties are very large. Recently, low-energy fission yields (up 20–30 MeV excitation) were obtained by bombarding a Pb target with 750 AMeV $^{238}$U [41]. In the case of Te isotopes, these data are compared with the $^{238}$U simulations at $E^* = 3, 20, 30, 50, 75$ and 100 MeV in fig. 14. In this selected range, an agreement of up two orders of magnitude is obtained between experiment and theory (30 MeV theoretical data). At $E^* = 3$ MeV, in average 1 neutron is evaporated and that causes an amplification of the odd-nuclei yields. At higher energies, the even isotopes yields are favoured. The agreement between experimental and theoretical values is rather good having in mind the assertion [42] that quantitative agreements over 20 orders of magnitude for *ab initio* calculations concerning the isotopic distributions are remarkables.

It is important to confront the trends exhibited by the products yields as a function of the excitation energy with available data. In ref. [43], accurate measurements of Rb and Cs $^{238}$U fission products yields were obtained for 40, 50 and 60 MeV bombarding protons. Such data, determined with incident charged particles, supply reliable information concerning the isotopic distribution as a function of the kinetic energy of the incident beam. The variations of the average $\langle A \rangle$ values

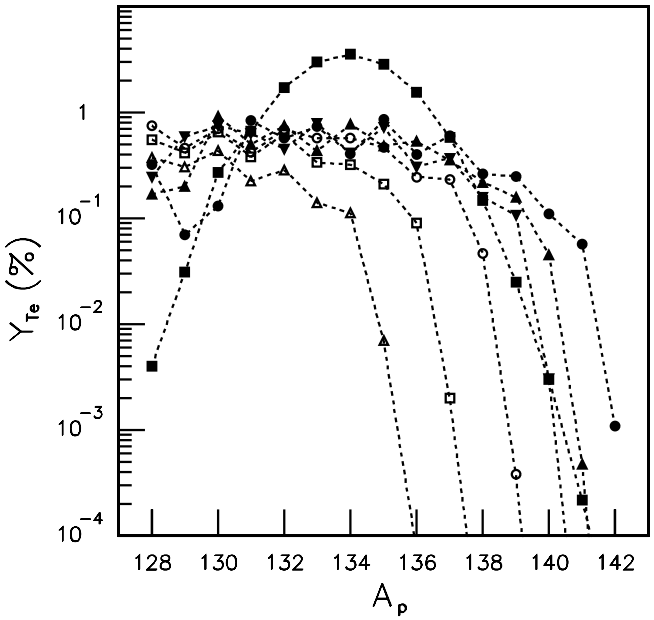


**Fig. 14.** Isotopic products yields for Te. The filled squares represent the data for low-energy fission of $^{238}$U while the filled circles are from the theoretical distribution for the same nucleus for $E^* = 3$ MeV, the up-point filled triangles for $E^* = 20$ MeV, the down-point filled triangles for $E^* = 30$ MeV, the empty circles for 50 MeV, the empty squares for 75 MeV and the empty triangles for 100 MeV.

of Rb and Cs isotopes with the incident proton energies are considered as a basis for our comparisons. Also, it is considered that the incident kinetic energy offers a good estimation of the compound nucleus excitation. From ref. [43], $\Delta\langle A_{\rm Rb}\rangle/\Delta E_{\rm kin} \approx -0.01395$ u/MeV and $\Delta\langle A_{\rm Cs}\rangle/\Delta E_{\rm kin} \approx -0.02825$ u/MeV at an incident proton kinetic energy $E_{\rm kin} = 50$ MeV. For $E^* = 50$ MeV, the theoretical product distributions of $^{238}$U fission give $\Delta\langle A_{\rm Rb}\rangle/\Delta E^* \approx -0.0542$ and $\Delta\langle A_{\rm Cs}\rangle/\Delta E^* \approx -0.06387$. This behavior indicates that the model shifts faster the isotopic yield distributions towards the stability line in comparison with the experimental findings.

## 3 Fission products yields

In the following, fission product yields obtained in the target are determined as a function of the initial deuteron energy for a specific converter-target geometry. In this section, $E_d$ means the incident deuteron energy and $E_n$ the neutron energy.

### 3.1 Neutron distributions

The neutron angular $P(\theta, E_d)$ and energy distributions $P(\theta, E_n, E_d)$ produced in the converter depend strongly on the initial deuteron energy $E_d$. Increasing the deuteron energy, the neutron flux in the forward direction increases rapidly up to $E_d \approx 100$ MeV. From $E_d = 100$ MeV a saturation effect is visible. This effect causes an increase of the neutron yields at almost all energies, including the range 0–20 MeV where the neutron-rich isotopes produced by fission can survive.

Angular and energy distributions of neutrons obtained by bombarding thick targets with incident deuterons up to 200 MeV are reported [44–46], scanning a large energy interval where quantitative data were not available. A simple phenomenological formalism intended to simulate the distributions in the forward direction was developed and presented in detail in ref. [45] by extending the formalism based on Serber's theory [47]. The experimental results compared with phenomenologic simulations proved to be in good agreement. Following the Serber's prescriptions, two distributions can be modelized semi-classically in the case of thin targets: one distribution is due to the stripping reaction and another is due to direct collisions between nucleons, resulting in the escape of some particles from the target nucleus. For an initial deuteron energy, these distributions determine the neutron probability $P(\theta, E_n, E_d)$ to be emitted at an angle $\theta$ at an energy $E_n$. In the case of thick targets, this probability must be integrated over the deuteron range weighted with the cross-section $(d, n)$. The theoretical angular and energy neutron yields were finally obtained by renormalization of the integrated probability with the experimental value of the total yield at 0°. This formalism needs, first of all, an estimation of the neutron yields at 0° for thick Be targets as a function of the deuterons incident energies. This dependence gives the approximate productivities for other kinds of targets by using simple geometric relations involving the atomic and mass numbers of the concerned elements. Semi-empirical formulae for this quantity (neutron yields at 0°) are given in ref. [48] (for incident energies smaller than 15 MeV) and ref. [49] (over 15 MeV), but their validity becomes uncertain for deuteron energies greater than 50 MeV due to the lack of experimental data over this value. Using the experimental yields obtained in refs. [44–46], together with a systematic of experimental data, a fit of the data has been made and the following formula is proposed for the yields at 0° up to 200 MeV deuteron incident energy on thick Be targets

$$\Phi(\theta = 0^\circ) = \begin{cases} 10.1 \times 10^{12} E_d^{2.95}, & \text{for} \quad E_d < 15 \text{ MeV}, \\ 3.4 \times 10^{13} E_d^{2.5}, & \text{for} \quad 15 \text{ MeV} \le E_d \le 50 \text{ MeV}, \\ \left\{ \frac{928.3}{1+\exp[0.053(98-E_d)]} - 6.89 \right\} \times 10^{16}, & \text{for} \quad 50 \text{ MeV} < E_d \end{cases} \tag{35}$$

where $\Phi$ is the number of neutrons over the incident charge unit in $\mathrm{sr}^{-1}\mathrm{C}^{-1}$ and the incident energy of the deuteron $E_d$ is given in MeV. The experimental systematic and the empirical parametrization are displayed in fig. 15.

Our estimations require the cross-section for neutron production in order to weight along the target thickness. One choice for the dependence of the forward direction cross-section in the Be target is given by the formula [50]

$$\left.\frac{\mathrm{d}\sigma(E)}{\mathrm{d}\Omega}\right|\theta = 0^\circ = 0.18 \ln(E) + 0.007E \tag{36}$$

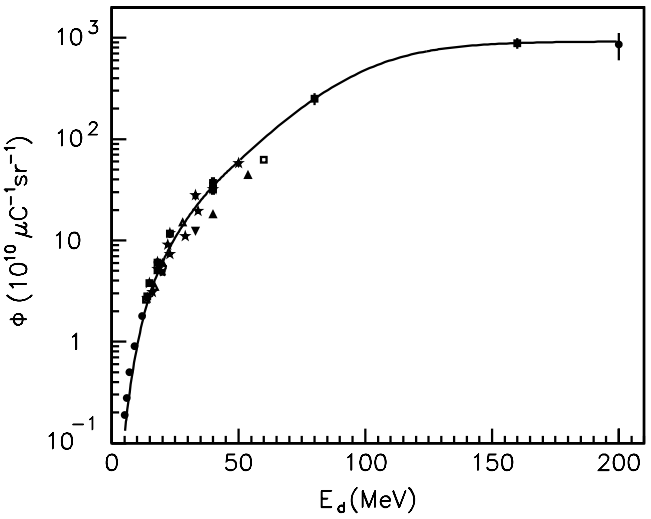


**Fig. 15.** A systematic of total yields $\Phi$ at 0° *vs.* the incident energy of the deuteron $E_d$ for the bombardment of Be is obtained by plotting experimental results given in different references: filled circles from ref. [49] (5, 6, 7, 9, 12, 18 and 23 MeV), filled squares from ref. [50] (14, 14.8, 18, 23 and 40 MeV), up-point filled triangles deduced from ref. [51] (40 and 53.8 MeV), down-point filled triangle from ref. [52] (12.5 MeV), empty circle from ref. [53] (20.2 MeV), empty square from ref. [48] (13.54 MeV), up-point empty triangles from [45] (17, 20 and 28 MeV), empty rhombs from ref. [54] (16, 33 and 50 MeV), empty crosses from ref. [55] (4 points at 40 MeV), filled stars from the compilation of ref. [56] (14, 16, 18, 22, 23, 29, 33, 34, 40 and 50 MeV), empty stars from ref. [57] (14.8, 18 and 23 MeV), asterisk from ref. [58] (20 MeV), filled circle at $E_d = 200$ MeV from ref. [46], empty square at 60 MeV deduced from ref. [59], filled squares at 80 and 160 MeV from ref. [44]. In the low-energy deuteron energy the plot looks like with the curve drawn in ref. [60]. The curve is obtained with the semi-empirical parametrization given by relation (35).

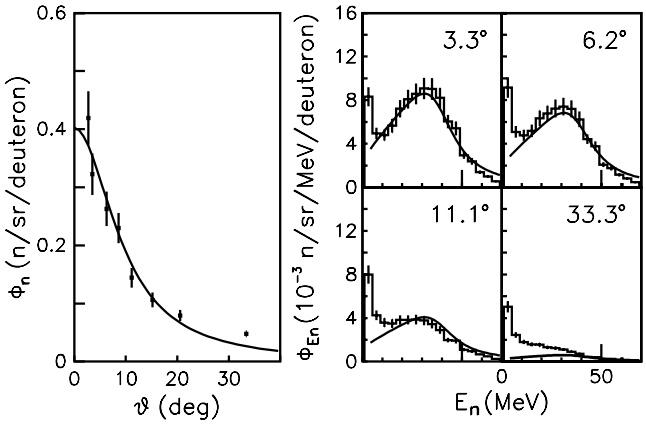


**Fig. 16.** Left part: angular neutron distribution $\Phi_n$ *vs.* the direction angle $\theta$ for Be target. The filled squares correspond to the deuteron incident energy $E_d$= 80 MeV. Right part: neutron energy distributions $\Phi_{E_n}$ at different detection angles (marked on the plots). The full curve represents the simulations.

and another proposed dependence [45] as

$$\left.\frac{\mathrm{d}\sigma(E)}{\mathrm{d}\Omega}\right|\theta = 0^\circ \ = 2. \times 10^{-4} E^{1.5} \left|\frac{\mathrm{d}E}{\mathrm{d}t}\right|, \qquad (37)$$

where $\mathrm{d}E/\mathrm{d}t$ is the stopping power in MeV/(g/cm$^2$), $E$ is the deuteron energy in MeV for the range $t$ in the target, and the cross-section is expressed in b/sr. Both approximations were used in calculations up to 40–50 MeV deuteron energies. In the following, the dependences exhibited by these formulae were extrapolated for all the energy domain concerned with the imposed restriction that when $\sigma$ reaches the value 1.35 b, this value being regarded as an upper limit [59], $\sigma$ remains constant. In this context, it was considered that at the highest energies, the major part of the cross-section is concentrated in the forward direction. The theoretical simulations for incident deuteron at energies of 80 and 160 MeV obtained by using these two parametrizations (relations (36) and (37)) were almost identical. Also, as usually done for thick targets, an attenuation of the initial beam was taken into account by multiplying the cross-section with a factor directed by a law of the type $\exp(-\int N\sigma\ \mathrm{d}t)$, where $\int N\ \mathrm{d}t$ is the number of nuclei on the surface unit. Another modification of the formalism of ref. [45] is that the straggling angle is computed by extrapolating the table of ref. [61] as a function of the deuteron position in the target, while in our previous work [45] the mean value over the range of the deuteron was considered.

In fig. 16, a comparison between the experimental and theoretical distributions obtained in ref. [44] for an incident deuteron energy of 80 MeV is displayed. This comparison offers an idea about the degree of accuracy obtained in computing the neutron distributions.

### 3.2 Number of fission events

The dimensions of the $^{238}$U fissionable target are small, so that it is possible to neglect the attenuation of the neutrons in the uranium. The geometry illustrated in fig. 17 will be considered in the following because it is the most often geometry used in practice. The set-up consists of two cylindrical pieces: the converter and the fissionable target positioned horizontally along the deuteron beam direction. Usually, the target is made from uranium carbide $UC_x$. The converter delivers the neutrons obtained mainly by break-up processes as mentioned previously. Using the above theoretical distributions $P(\theta, E_n, E_d)$ and $P(\theta, E_d)$, a mean distance of the neutrons emitted from a slice of the converter in the fissionable target can be calculated

$$R_m = \frac{4\int_0^{R_c}\int_0^{\sqrt{R_c^2-y^2}} d_m(x,y)\mathrm{d}x\mathrm{d}y}{\pi R_c^2}, \qquad (38)$$

where

$$d_m(x,y) = \frac{\int_0^{2\pi}[\int_0^{\pi/2} P(\theta,E_d)\mathrm{d}(\theta,\varphi)\sin(\theta)\mathrm{d}\theta]\mathrm{d}\varphi}{2\pi\int_0^{\pi/2}\sin(\theta)P(\theta,E_d)\mathrm{d}\theta} \qquad (39)$$

is the mean range of the neutron in $^{238}$U emitted in a point $(x, y)$ in the converter and $d(\theta, \varphi)$ is the range of the

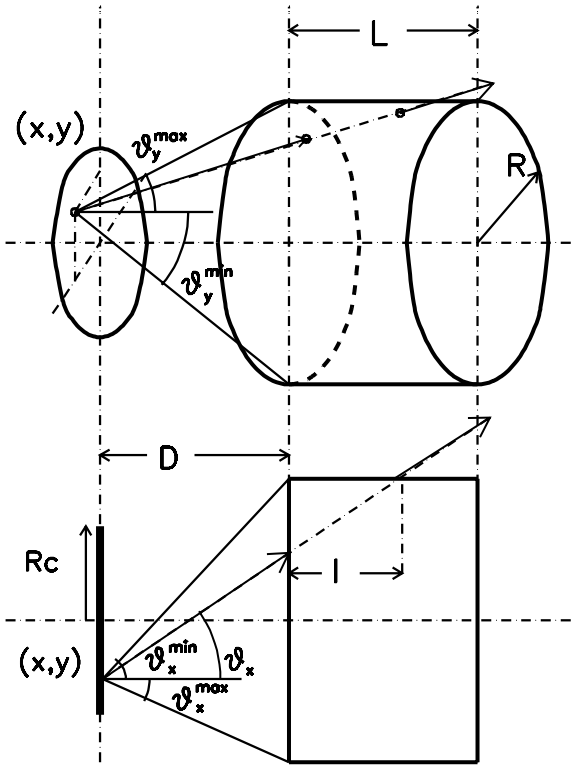


**Fig. 17.** The experimental schematic set-up. Top: perspective vue and bottom: section along the symmetry axis. $(x, y)$ represents a point in one slice of the converter where the deuteron is broken and a neutron emerges at angles $\theta_x$ and $\theta_y$. The maximal values of these angles allowing that the neutron hits the target are also represented. $D$ is the distance between the slice of the converter and the entry edge of the target, $L$ is the thickness of the cylindrical target, $R$ is the radius of the target, $R_c$ is the radius of the converter (which equals the radius of the beam).

neutron emitted at the angles $\theta$ and $\varphi$. $R_c$ represents the radius of the converter, considered equal to that of the incident deuteron beam. The values of $d(\theta, \varphi)$ are computed using geometrical relations. It was considered easier to replace the variables $\theta$ and $\varphi$ with $\theta_x$ and $\theta_y$ fulfilling the condition of the same angular domain

$$\int_0^{2\pi}\left[\int_0^{\pi/2} P(\theta, E_d)d(\theta,\varphi)\sin(\theta)\mathrm{d}\theta\right]\mathrm{d}\varphi = \int_{-\pi/2}^{\pi/2}\int_{-\pi/2}^{\pi/2} P(\theta[\theta_x,\theta_y], E_d)d(\theta_x,\theta_y)\sin(\theta[\theta_x,\theta_y]) \times\mathcal{D}\left(\frac{\theta,\varphi}{\theta_x,\theta_y}\right)\mathrm{d}\theta_x\mathrm{d}\theta_y, \quad (40)$$

where

$$\theta(\theta_x,\theta_y) = \arctan\left\{\left[\tan^2(\theta_x)+\tan^2(\theta_y)\right]^{1/2}\right\}, \quad (41)$$

$$\varphi(\theta_x,\theta_y) = \arctan\left(\frac{\tan(\theta_x)}{\tan(\theta_y)}\right) \quad (42)$$

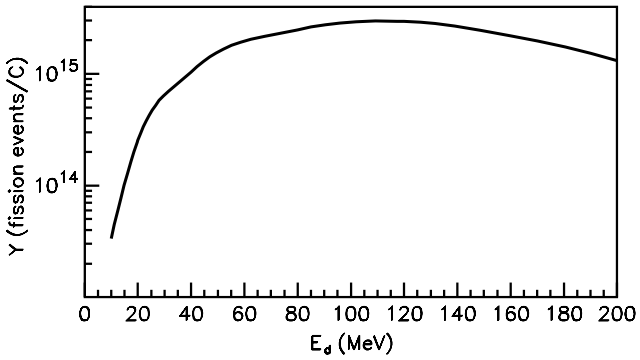


**Fig. 18.** The number of fission events $Y$ able to produce neutron-rich nuclear fragments per incident charge of deuteron as a function of the deuteron energies $E_d$.

and the Jacobi determinant is

$$\mathcal{D}\left(\frac{\theta,\varphi}{\theta_x,\theta_y}\right) = \left|\frac{\mathrm{d}\theta}{\mathrm{d}\theta_x}\frac{\mathrm{d}\varphi}{\mathrm{d}\theta_y} - \frac{\mathrm{d}\theta}{\mathrm{d}\theta_y}\frac{\mathrm{d}\varphi}{\mathrm{d}\theta_x}\right|. \quad (43)$$

The significance of $\theta_x$ and $\theta_y$ can be found inspecting fig. 17. In these calculations, it is considered that the neutrons are emitted in a weighted position in the converter

$$R_p = \frac{\int_0^T \sigma[E(t)]t\mathrm{d}t}{\int_0^T \sigma[E(t)]\mathrm{d}t}, \quad (44)$$

where $\sigma[E(t)]$ represents the cross-section for neutron production at the depth $t$ in the converter and $T$ is the thickness of the converter.

Now, the total number of fission events can be approximatively estimated by charge unit of incident deuteron

$$N_f(E_d) = \frac{R_m N_t \rho_U}{M_U}\frac{\int_0^{E_d}\sigma_f(E)D(E,E_d)\mathrm{d}E}{\int_0^{E_d}D(E,E_d)\mathrm{d}E}, \quad (45)$$

where

$$D(E_n,E_d) = 2\pi\int_0^{\pi/2} P(\theta,E_n,E_d)\sin\theta\mathrm{d}\theta \quad (46)$$

is an average energy distribution of the neutrons, $\sigma_f(E)$ is the fission cross-section, $\rho_U$ is the U density, $M_U$ is the U mass, $D(E, E_d)$ is the neutron energetic distribution. The total number $N_t$ of neutrons emitted by the converter is

$$N_t = 2\pi\int_0^{\pi/2} P(\theta,E_d)\sin(\theta)\mathrm{d}\theta. \quad (47)$$

For a given geometry, these formulae allow us to estimate the number of fission events in the target. If the cross-section is multiplied with the products distributions normalized to 200% obtained at each neutron energy, we are able to determine the isotopic number of elements produced for an incident deuteron energy $E_d$.

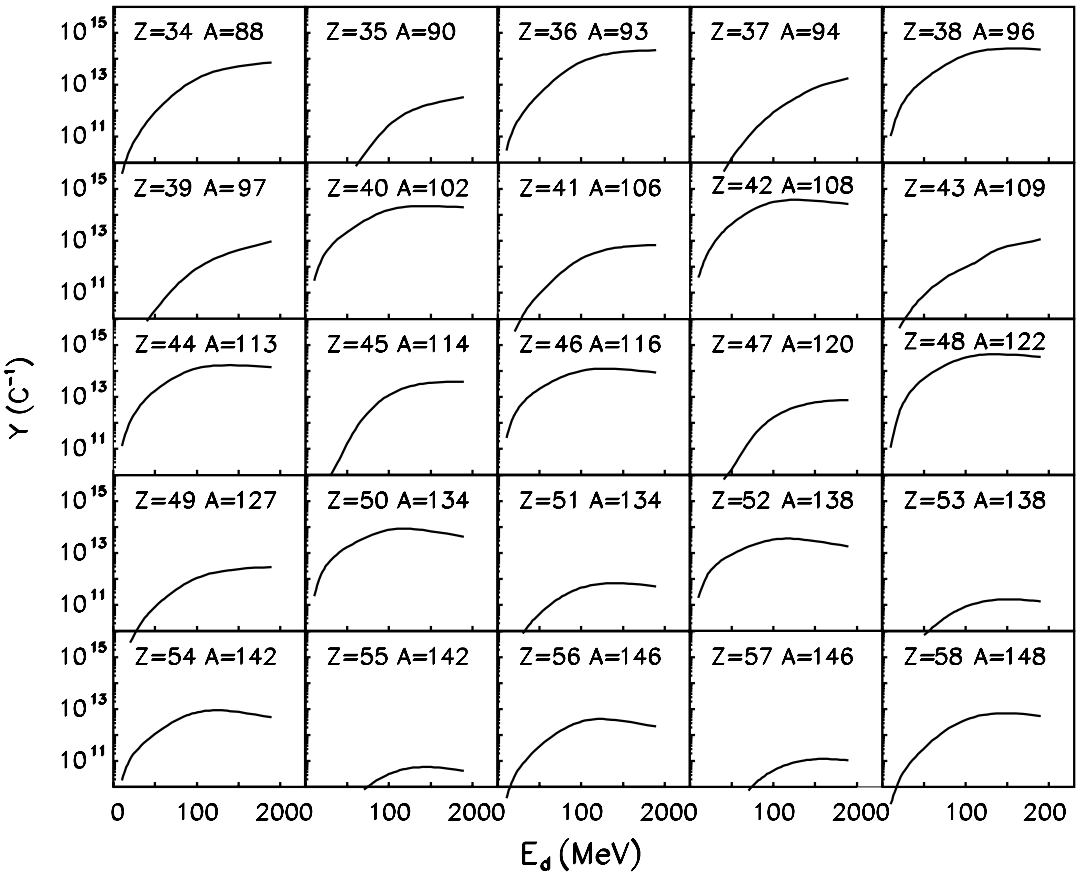


**Fig. 19.** The number of fission products $Y(A_p, Z_p)$ per incident charge of deuteron as a function of the deuteron energies $E_d$ for several neutron-rich isotopes.

## 4 Results and discussion

The theoretical optimum deuteron energy will be obtained using two methods. First of all, a simple estimation of the deuteron energy required to produce the largest number of unstable products is obtained by taking into account only the neutron distributions and some simple assumptions concerning the fission. The second estimation takes into account the isotopic product distributions and the variation of the excitation energy due to the incident neutron binding energy in the compound $^{239}$U nucleus.

If the energy of the neutron is too high, the fragment emits neutrons, so that it will be shifted towards the stability line. It was shown in refs. [1,7] that for excitation energies larger than 20 MeV, the formed neutron-rich fragments are too excited to survive. For example, analysing the experimental data displayed in fig. 14, at low excitations, the maximal yield is obtained for $A_p = 134$, while the neutron drip line is in the vicinity of $^{138}$Te. The yields decrease rapidly for isotopes heavier than $^{134}$Te. At excitations energies larger than 20 MeV, due mainly to the release of several neutrons, the yields are shifted towards stability. So, in order to have a first-order estimation, it will be considered that only fission events produced at $E^* < 20$ MeV produce neutron-rich products able to survive. In this first-order estimation, we neglect momentary the nuclear structure of the parent nucleus by considering that the initial kinetic energy of the bombarding neutron equals the excitation energy. Including the following approximation in the numeric code

$$\sigma(E) \to \left[1 - \mathcal{H}\left(\frac{E - E_0}{E_0}\right)\right] \sigma(E), \qquad (48)$$

the number of fragments produced the fission induced by neutrons with incident kinetic energies lower than 20 MeV can be obtained. Here, $\mathcal{H}(x)$ is the Heaviside function with the properties that $\mathcal{H}(x) = 0$, when $x < 0$ and $\mathcal{H}(x) = 1$, when $x \geq 0$ and $E_0 = 20$ MeV. That means, only fission fragments obtained at energies smaller than 20 MeV neutrons are retained. However, the angular and energy neutron distributions in the 0–20 MeV range present a strong dependence on the initial duteron energy. This procedure enables us to extract an approximate value of the best deuteron energy.

In the following estimations, the converter thickness was always chosen to equalize the $^2$H range at each incident energy. The radius of the $^{238}$U cylinder was 7 mm, its thickness is 60 mm and it was considered to be built

from $UC_x$. The distance between the exit edge of the converter and the entrance face of the $^{238}$U target correspond to 10 mm. The converter was considered to be built from C. The deuteron beam radius equals 1 mm.

In fig. 18, the number of fission events able to produce neutron-rich fragments per charge of incident deuterons is plotted as a function of the deuteron energy. It can be observed that the maximum number of interesting fission events is produced when the $^2$H has an energy close to 100 MeV. In the same time, the yield does not increase very much in the interval 60 MeV to 100 MeV, and it will be more convenient to construct an accelerator for $^2$H at 60 MeV, due to the costs of such a facility.

In the following, in connection with the previous fixed converter-target geometry, the number of fission products produced in the uranium target per deuteron incident charge will be determined. The neutron-rich isotopes of Se up to Ce will be analysed. In the frame of this second estimation method, the structure of the parent nucleus is taken into consideration trough the mass defect evaluation and without imposing the condition (48). In this context, firstly, the excitation energy of the uranium target must be determined.

The excitation energy is estimated crudely in connection with the incident neutron energy. If the compound $^{239}$U nucleus is formed, the excitation energy deposited by the neutron is considered equal to its incident energy plus the variation of the mass defect of the $^{239}$U nucleus *vs.* that of the $^{238}$U+n system: $Q_{\rm BE} = M(^{238}{\rm U}) + m_n - M(^{239}{\rm U}) =$ 4.8 MeV. Having in mind that this variation is about 4.8 MeV, and that we are concerned by the influence of the excitation energy in a wide range of neutron energies, up to hundreds of MeV, it can be assessed that for our purpose this variation of the mass defect has little influence. In the case of $^{238}$U residual nucleus, the energy of the recoil neutron was considered as approximatively 3 MeV and the excitation energy deposited in the $^{238}$U of about $E_n - 3$ MeV.

The cross-section curve exhibits a threshold behavior characterized by a second step that occurs at a bombarding energy of about 6-7 MeV. This is the threshold for a "second chance fission" where the $^{239}$U compound nucleus can emit a neutron and the residual $^{238}$U nucleus undergoes fission. Therefore, neglecting other fission channels, the fission cross-section is divided in two components: a cross-section for $^{239}$U with the threshold at approximatively 1 MeV and a maximum value of $\approx 0.5$ b and a cross-section for the $^{238}$U with the threshold at 6 MeV and a maximum value of $\approx$0.5 b. The total fragment distribution is obtained by overlapping these two distributions.

The number of products $Y(A_p, Z_p)$ produced in the $^{238}$U fission target by charge of incident deuterons are displayed in fig. 19 as a function of the incident energy $E_d$. Only one value of the mass number $A_p$ is selected for isotopes with half-lives near to one or several seconds. A very pronounced odd-even effect in the atomic number $Z_p$ can be remarked. First, the even fragments will be discussed. It can be evidenced that, as previously remarked, for $E_d \approx 100$ MeV, the number of neutron-rich nuclei supplied by the facility reaches values close to the maximal ones. In the case of light elements, in the vicinity of $E_d = 100$ MeV, the slope of the curves decreases dramatically and a saturation behavior begins to be evidenced for larger values of the incident deuteron energy. Concerning the heavy products, it is interesting to note that even their yields begin to decrease slowly for $E_d$ energies above 100 MeV. In almost all cases, the increase of the neutron-rich product yields from 60 to 100 MeV is lower than one order of magnitude. In the case of odd $Z_p$, the maximal values of the yields are attained for higher $E_d$ than for even $Z_p$. In this case, the increase of the potential barrier due to single-particle effects is greater and these microscopical effects vanish at larger excitation energy of the parent.

In the frame of the PARRNe project, the production of noble gases was investigated experimentally using a $UC_x$ cylindrical fissionable target containing about 30 g of uranium. Experiments were realised at 80 and 130 MeV deuteron energies using the AGOR cyclotron at KVI Gröningen [62]. The noble gases were transported through a transfer line in order to be collected on a cold finger. The resulting activity was measured under good background conditions by $\gamma$-spectroscopy. Comparisons with the theory will be realised under the assumption that the number of isotopes detected is proportional to the number of fission products (of the same isotope) produced in the fission target. Therefore, the ratios between the experimental yields measured at $E_d = 130$ MeV and 80 MeV were computed. We obtained 1.91, 1.5, 1.3 and 1.53 for $^{89}$Kr, $^{137}$Xe, $^{138}$Xe and $^{139}$Xe, respectively. The theoretical values of the ratios of the yields produced in the fission target at the same energies were 5.04, 2.00, 1.78 and 2.05 for the same isotopes, respectively. Quantitatively, the calculated and the theoretical values in the case of Xe isotopes show a remarkable agreement. Qualitatively, the theory evidences that the increase of the Kr yield is more pronounced with the deuteron energy than those of the Xe isotopes. Relatively to the even Xe isotope, the increase of the odd Xe yields is more pronounced, both theoretically and experimentally. The theory, in connection with the experimental data, shows that increasing the energy above $E_d = 80$ MeV, the increase of the neutron-rich isotope yields is not too consistent.

These calculations suggest that without expensive facilities, a large number of isotopes far from the stability line can be obtained at a deuteron energy of 60 MeV. Our estimations take into account the angular and energy distributions of neutrons produced in the converter, the excitation of the fission nucleus which modifies the channel partition $(A_1, Z_1, A_2, Z_2)$ probabilities and the neutron evaporation.

This work was sponsored by the European Contracts SPIRAL II No. ERB 4062 PL 975009, No. FMGE CT 980100 and by the IDRANAP European Center of Excellence.

## References


1. I.C. Gomes, J.A. Nolen, in *Proceedings of the II International Topical Meeting on Nuclear Applications of Accelerator Technology, Gatlinburg, TN, USA, September 20–23, 1998*; J.A. Nolen, private communication, 1998.
2. F. Clapier, A.C. Mueller, C. Obert, O. Bajeat, M. Ducourtieux, A. Ferro, A. Horbowa, L. Kotfila, C. Lau, H. Lefort, S. Kandry-Rody, N. Pauwels, J.C. Poitier, J. Proust, J.C. Putaux, C.F. Liang, P. Paris, A.C.C. Vilari, R. Lichtenhäler, L. Maunoury, J. Lettry, Phys. Rev. ST Accel. Beams **1**, 013501 (1998).
3. S. Kandri-Rody, J. Obert, E. Cottereau, O. Bajeat, M. Ducourtieux, C. Lau, H. Lefort, J.C. Poitier, J.C. Putaux, F. Clapier, J. Lettry, A.C. Mueller, N. Pauwels, J. Proust, C.F. Liang, P. Paris, H.L. Ravn, B. Roussiere, J. Sauvage, J.A. Scarpaci, F. Le Blanc, G. Lalu, I. Lhenry, T. Von Egidy, R. Antoni, Nucl. Instrum. Methods B **160**, 1 (2000).
4. R. Bennet, P. Van Duppen, H. Geissel, K. Heyde, B. Jonson, O. Kester, G.-E. Körner, W. Mittig, A.C. Mueller, G. Münzenberg, H.L. Ravn, K. Riisager, G. Schrieder, A. Shotter, J.S. Vaagen, J. Vervier, NuPECC Report 2000, (`http://www.nupecc.org`).
5. D. Ridikas, W. Mittig, A.C.C. Villari, in *International Conference on Shielding Aspects of Accelerators, Targets and Irradiation Facilities (SATIF 5)* (Paris, 17–21 July 2000, OECD), to be published.
6. A.C. Wahl, in *Symposium on Physics and Chemistry of Fission, Salzburg 22–26 March*, Vol. **1** (IAEA, Vienna, 1965) p. 317.
7. M. Mirea, F. Clapier, N. Pauwels, J. Proust, Nuovo Cimento A **111**, 267 (1998).
8. W.J. Swiatecki, S. Bjornholm, Phys. Rep. **4**, 324 (1972).
9. K. Depta, R. Hermann, J.A. Maruhn, W. Greiner, in *Dynamic of Collective Phenomena*, edited by P. David (World Scientific, Singapore, 1987) p. 29.
10. K. Depta, J.A. Maruhn, Hou-Ji Wang, A. Săndulescu, W. Greiner, Int. J. Mod. Phys. A **5**, 3901 (1990).
11. M. Mirea, D.N. Poenaru, W.Greiner, Z. Phys. A **349**, 39 (1994).
12. M. Mirea, D.N. Poenaru, W. Greiner, Nuovo Cimento A **105**, 571 (1992).
13. M. Brack, J. Damgaard, A. Jensen, H. Pauli, V. Strutinsky, W. Wong, Rev. Mod. Phys. **44**, 320 (1972).
14. K.T.R. Davies, J.R. Nix, Phys. Rev. C **14**, 1977 (1976).
15. D.N. Poenaru, M. Ivaşcu, D. Mazilu, Comput. Phys. Commun. **19**, 205 (1980).
16. P. Möller, J.R. Nix, At. Data. Nucl. Data Tables **26**, 165 (1981).
17. J. Maruhn, W. Greiner, Z. Phys. **251**, 431 (1972).
18. M. Mirea, Phys. Rev. C **54**, 302 (1996).
19. M.Mirea, F. Clapier, Europhys. Lett. **40**, 509 (1997).
20. M. Mirea, Phys. Rev. C **57**, 2484 (1998).
21. M. Mirea, Eur. Phys. J. A **4**, 335 (1999).
22. M. Mirea, Phys. Rev. C **63**, 034603 (2001).
23. E. Badralexe, M. Rizea, A. Săndulescu, Rev. Roum. Phys. **19**, 63 (1974).
24. P. Holzer, U. Mosel, W. Greiner, Nucl. Phys. A **138**, 241 (1969).
25. S.G. Nilsson, Chin Fu Tsang, A. Sobiczewski, Z. Szymansky, S. Wycech, C. Gustafson, I.-L. Lamm, P. Möler, B. Nilsson, Nucl. Phys. A **131**, 1 (1969).
26. V.M. Strutinsky, Nucl. Phys. A **122**, 1 (1968).
27. F.A. Ivanyuk, M.S. Ivascu, D. Poenaru, in *Particle Emission from Nuclei*, edited by D.N. Poenaru, M.S. Ivascu, Vol. **1**, Chapt. 6 (CRC Press, Boca Raton, Florida, 1989) p. 168.
28. D.L. Hill, J.A. Wheeler, Phys. Rev. **89**, 1102 (1953).
29. H.J. Lustig, J.A. Maruhn, W. Greiner, J. Phys. G **6**, L25 (1980).
30. R.K. Gupta, W. Greiner, in *Heavy Elements and Related New Phenomena*, edited by W. Greiner, R.K. Gupta, Vol. **1**, Chapt. 14 (World Scientific, Singapore, 1999) p. 551.
31. K.T.R. Davies, A.J. Sierk, J.R. Nix, Phys. Rev. C **13**, 2385 (1973).
32. D.N. Poenaru, M. Ivascu, I. Ivascu, M. Mirea, W. Greiner, K. Depta, W. Renner, in *International Conference 50 Years with Nuclear Fission*, edited by J.W. Behrens, A.D. Carlson (American Nuclear Society, Lagrange Park, 1989) p. 617.
33. D.N. Poenaru, M. Mirea, W. Greiner, I. Cata, D. Mazilu, Mod. Phys. Lett. A **5**, 2101 (1990).
34. T. Benfoughal, M. Mirea, J. Phys. III **6**, 1403 (1996).
35. T. Ledergerber, H.C. Pauli, Nucl. Phys. A **207**, 1 (1973).
36. H.C. Pauli, Nucleonika **20**, 601 (1975).
37. W.D. Myers, W.J. Swiatecki, Nucl. Phys. A **601**, 141 (1996).
38. E. Segré, in *Nuclei and Particle* (W.A. Benjamin, Inc., New York, 1964) Chapt. 11, p. 494.
39. J. Terrel, Phys. Rev. **127**, 880 (1962).
40. F. Gönnenwein, in *Proceedings of the XIII International Symposium on Nuclear Physics: Physics and Chemistry of Fission at Castle Gaussig, GDR, 21-25 Nov. 1988*, edited by. H. Märten, D. Seeliger (Zentral Institut Kernforschung Rossendorf, Dresden, 1998) Rossendorf Report zfk-732.
41. C. Donzaud, S. Czajkowski, P. Armbruster, M. Bernas, C. Böckstiegel, Ph. Dessagne, H. Geissel, E. Hanelt, A. Heinz, C. Kozhuharov, Ch. Miehé, G. Münzenberg, M. Pfützner, W. Schwab, C. Stéphan, K. Sümmerer, L. Tassan-Got, B. Voss, Eur. Phys. J. A **1**, 407 (1998).
42. W. Greiner, in *Advances in Nuclear Physics*, edited by D.N. Poenaru, S. Stoica (World Scientific, Singapore, 2000).
43. B.L. Tracy, J. Chaumont, R. Klapisch, J.M. Nitschke, A.M. Poskanzer, E. Roeckl, C. Thibault, Phys. Rev. C **5**, 222 (1972).
44. N. Pauwels, S. Brandenburg, H. Laurent, J.P.M. Beijers, F. Clapier, L. Lebreton, M. Mirea, M.G. Saint-Laurent, R.G.T. Zegers, Preprint IPNO 00–01, 2000, unpublished.
45. S. Menard, M. Mirea, F. Clapier, N. Pauwels, J. Proust, C. Donzaud, D. Guillemaud-Mueller, I. Lhenry, A.C. Mueller, J.A. Scarpaci, O. Sorlin, Phys. Rev. ST Accel. Beams **2**, 033501 (1999).
46. N. Pauwels, F. Clapier, P. Gara, M. Mirea, J. Proust, Nucl. Instrum. Methods B **160**, 315 (2000).
47. R. Serber, Phys. Rev. **72**, 1008 (1947).
48. H.J. Brede, G. Dietze, K. Kudo, U.J. Schrewe, F. Tancu, C. Wen, Nucl. Instrum. Methods A **274**, 332 (1989).
49. M.A. Lone, A.J. Ferguson, B.C. Robertson, Nucl. Instrum. Methods **189**, 515 (1981).
50. D. Christenson, M.W. McNaughton, J.A. Jungerman, Nucl. Instrum. Methods **160**, 499 (1979).
51. G.W. Schweimer, Nucl. Phys. A **100**, 537 (1967).
52. Kazuo Shin, Kouki Hibi, Masahito Fujii, Yoshitomo Uwamino, Takashi Nakamura, Phys. Rev. C **29**, 1307 (1984).

53. A. Belymam, A. Hoummada, J. Collot, P. de Saintignon, G. Mahout, B. Merkel, Nucl. Instrum. Methods B **134**, 217 (1998).
54. J.P. Meulders, P. Leleux, P.C. Macq, C. Pirart, Phys. Med. Biol. **20**, 235 (1975).
55. M.J. Saltmarsh, C.A. Ludemann, C.B. Fulmer, R.C. Styles, Nucl. Instrum. Methods **145**, 81 (1977).
56. P. Grand, A.N. Goland, Nucl. Instrum. Methods **145**, 49 (1977).
57. M.A. Lone, C.B. Bigham, J.S. Fraser, H.R. Schneider, T.K. Alexander, A.J. Ferguson, A.B. McDonald, Nucl. Instrum. Methods **143**, 331 (1977).
58. J. Collot, P. De Saintignon, P. Gabor, A. Hoummada, G. Mahout, D. Marchand, F. Merchez, E. Leon Florian, C. Leroy, Ph. Jean, B. Merkel, Nucl. Instrum. Methods A **350**, 532 (1994).
59. K. Goebel, A.J. Miller, Nucl. Instrum. Methods **96**, 581 (1971).
60. J.A. Stokes, L.A. Parks, C.A. Preskitt, J. John, IEEE Trans. Nucl. Sci. **NS–30**, 1623 (1983).
61. H. Bichsel, Preprint USC–136–150, 1970.
62. F. Ibrahim et al., `http://www.ganil.fr/spiral2` (to be published).